LBL-24854
Preprint

# Lawrence Berkeley Laboratory
UNIVERSITY OF CALIFORNIA



Submitted to Physical Review C

## Stripping- and Pickup-induced Breakup in 11- and 17-MeV/nucleon $^{20}Ne$ + $^{197}Au$ Reactions

S.B. Gazes, H.R. Schmidt, Y. Chan,
E. Chavez, R. Kamermans, and R.G. Stokstad

March 1988



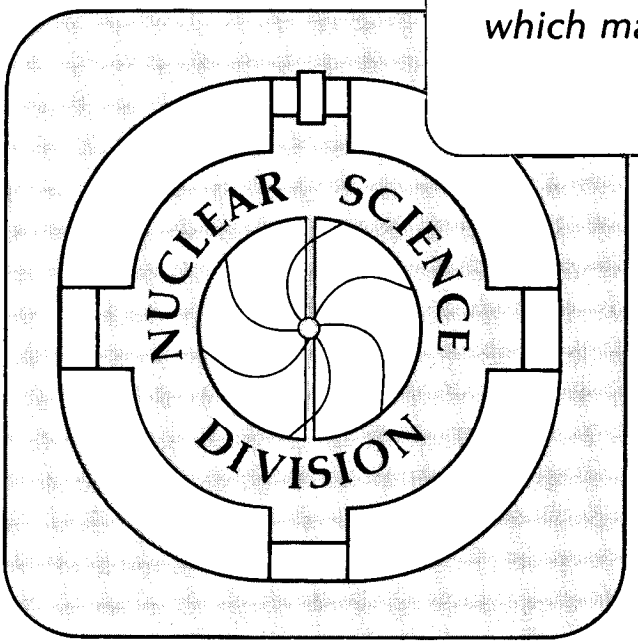


Prepared for the U.S. Department of Energy under Contract DE-AC03-76SF00098

## DISCLAIMER

LBL-24854

# Stripping- and pickup-induced breakup in 11- and 17-MeV/nucleon $^{20}Ne$ + $^{197}Au$ reactions

S.B. Gazes,[a] H.R. Schmidt,[b] Y. Chan, E. Chavez,[c] R. Kamermans,[d] and R.G. Stokstad

Nuclear Science Division, Lawrence Berkeley Laboratory,
University of California, Berkeley, California 94720

## Abstract

Breakup processes in 220- and 341-MeV $^{20}Ne$ + $^{197}Au$ reactions were studied by performing coincidence measurements of the secondary fragments. Projectile-like fragments and light charged particles corresponding to primary stripping, pickup, and inelastic channels were examined. The projectile-like fragments were detected near the classical grazing angle. Kinematic reconstructions of the three-body final states were used to deduce the excitations in the primary projectile-like and target-like fragments. At both bombarding energies, the stripping channels produced relatively cold ejectiles, with the excitation residing mostly in the target recoil. However, the pickup channels tended to leave the target cold, while populating higher excitations in the ejectile. The data are consistent with nucleon transfer as the dominant mode for generating excitation, with the partition of excitation energy between the fragments governed by the direction of the transfer. An extended version of the optimum-Q-value model of Siemens et al. predicts target-like excitations in good agreement with data at 11 MeV/nucleon, but with deviations occurring at 17 MeV/nucleon.


PACS: 25.70.Cd

## I. Introduction

The phenomenon of projectile breakup has been studied extensively in recent years. Initially, particle-inclusive measurements were used to investigate transfer processes by assuming that breakup was unimportant at energies below 20 MeV/nucleon, even though earlier measurements [1] had noted large yields of beam-like protons and alpha particles. Subsequent two-particle correlation work has revealed that, in the energy range 10-20 MeV/nucleon, sequential decay of an excited projectile-like fragment is an important mechanism for producing these fast light particles [2-8], and may strongly influence the inclusive yield.

An earlier work [9] reported on the relative importance of transfer and breakup in quasi-elastic reactions of $^{20}Ne$ + $^{197}Au$ at bombarding energies of 220 and 341 MeV. A $4\pi$ detector, the plastic box, registered the number of light charged particles emitted in coincidence with projectile-like fragments. The charged-particle multiplicity was found to be low (0 or 1), and was used as an indicator of the excitation energy produced in the primary projectile-like fragments.

This experiment provided an overview of the transfer and breakup processes in the range 10-20 MeV/nucleon, and also demonstrated the need for obtaining more information on the coincident light particles. Since the light particles are emitted predominantly in the ejectile direction, a $4\pi$ geometry is not essential. Therefore, a more detailed study of the energy and angular correlations could be undertaken while surrendering complete solid-angle coverage. In the present work, a large-solid-angle position-sensitive plastic phoswich array [10,11] is used for observing the light fragments emitted in the breakup of the primary fragments. With such an experimental setup, we have been able to obtain information on the

multiplicity and charge (Z=1,2) of the fragments accompanying a projectile-like fragment. The energy and position information has enabled the determination of the relative velocity between detected projectile-like and light fragments. This, in turn, is used to deduce, from two- and three-body kinematics, the excitation energy in the primary projectile-like and target-like nuclei. The channels we will consider in this paper are the few-nucleon stripping and pickup channels, as well as inelastic scattering of the projectile. Some aspects of this work have been discussed previously in Ref. 12.

In Sect. II, the experimental setup is described, with particular emphasis on the properties of the phoswich array. The coincidence data are presented in Sect. III and include the multiplicities and angular distributions of the associated protons and alpha particles. The reconstruction of the primary fragment yields from the two- and three-body data, and the relative importance of three-body channels, are considered in Sect. IV. In Sect. V, the kinematic reconstructions are discussed, and the reconstructed fragment excitations are presented. A general discussion of breakup probabilities and excitation-energy generation and partition is reserved for Sect. VI, with comparisons between experimental results and calculations based on optimum Q-values. A summary and conclusions are presented in Sect. VII.

## II. Experimental Setup

In order to obtain particle identification as well as position and energy information for the protons and alpha particles, we have used a large-solid-angle position-sensitive plastic phoswich array [10,11].

The array is made up of eight segments. Each segment is 20-cm long and 2.5-cm wide, and consists of 0.5-mm-thick NE-102 and 4.5-mm-thick NE-115 plastic scintillators. The detection and identification is accomplished by using the phoswich technique, whereby scintillators of different decay times are viewed by a single photomultiplier tube. The detector array is described in detail in Refs. 10 and 11. Corresponding to the thickness of the ΔE layer, the low-energy thresholds were 6 MeV for protons and 24 MeV for alpha particles.

The complete phoswich array, consisting of eight segments, forms a 20 x 20 $cm^2$ detection area. The segmentation provides position information in the other dimension as well as a multiple-hit capability. Thus, the array enables the determination of the charge, energy, two-dimensional position, and multiplicity of the charged particles over a large area.

The deployment of the array is indicated in Fig. 1, which shows the experimental configuration used in the work at 11 MeV/nucleon. A three-element silicon telescope, with detector thicknesses of 75, 75, and 1000 $\mu$m, was used to detect beam-like fragments emitted at $28^\circ$, which is slightly forward of the classical grazing angle at $32^\circ$ ($r_C$ = 1.4 fm). The middle of the phoswich array was colinear with the target and telescope, and positioned 25 cm from the former. It thus covered an in-plane angular range of 6 - $50^\circ$. Such a large solid angle made it possible to use the array as a "$4\pi$" device to veto breakup (by requiring that no light fragments be observed), as well as a highly efficient detector for studying breakup. A second telescope was positioned on the opposite side of the beam, symmetric to the first. The same-side telescope was mounted in such a way as to minimize shadowing of the array, thus maximizing the array's

efficiency as well as allowing the study of coincident events with small relative kinetic energies.

At the higher bombarding energy of 17 MeV/nucleon, the phoswich array covered the same angular region but the heavy-ion telescopes were positioned at ± 16°, slightly forward of the classical grazing angle at 17 MeV/nucleon (18°, $r_C$ =1.4 fm). The position of the phoswich enabled us to examine coincident light charged particles emitted in the region -50° to +50°, with a "hole" of ±6° about the beam. Since, at 341 MeV, a significant portion of the coincident alpha yield is lost, the array is no longer an efficient veto of breakup. Because of this, an analysis of the coincident yields at the higher bombarding energy is more dependent on simulations.

The 220- and 341-MeV $^{20}Ne$ beams were provided by the 88-Inch Cyclotron of the Lawrence Berkeley Laboratory. Large yields of $^{20}Ne^{6+}$ and $^{20}Ne^{7+}$ were produced by the ECR ion source, with the result that the experiments were typically limited by the count rate in the phoswich array.

## III. Experimental Results

### III. A. 220 MeV

The inclusive yield of projectile-like fragments of Z=3-10 is dominated by nuclei with beam-like velocities. This is also true of those ejectiles in coincidence with protons and alpha particles. The multiplicity, M, of light charged particles, as a function of the charge of the detected (secondary) ejectile is shown in Fig. 2. The inclusive yield of projectile-like fragments is dominated by M=0 events, i.e., those with no additional light charged particles. The coincidence yield, in turn, is dominated by alpha emission for secondary fragments with Z=3-8, and by

protons for fluorine ions (see Table 1). The relative yield of M=2 events is very small, with the largest case being $^{12}C$, where $2\alpha$ coincidences made up ~ 5% of the total coincidences.

The distribution of coincident light fragments among the eight segments of the phoswich array provides a crude angular distribution. Such a distribution is shown in Fig. 3, for alpha particles in coincidence with projectile-like nuclei of Z=5-8, detected in the same-side telescope at $28^{\circ}$. (Coincidences between phoswich array and opposite-side telescope were far weaker.) In each of the four distributions shown, the yield exhibits a relative minimum for the middle segments, #'s 4 and 5. Since the heavy-ion telescope is positioned between those two segments, part of this depletion is the result of shadowing by the detector and its housing. However, this is a relatively small effect, as will become apparent in Sect. V (where the relative-energy constructions are presented). In fact, most of this drop in yield reflects the angular distribution of breakup alpha particles in the rest frame of the associated parent nucleus. The drop in coincident yield for the outer-most segments represents the finite opening angle of the breakup "cone". Finally, the distribution of alpha particles in the eight segments is asymmetric about the middle (telescope) position, becoming progressively more asymmetric for lighter ejectiles.

The above features are understandable in terms of the kinematics of sequential decay if the angular distributions of the primary fragments are taken into account. A previous study of heavy-ion/alpha angular correlations [3] showed how a strongly forward-peaked primary angular distribution gives rise to an enhancement of coincident alpha particles at angles forward of the detected heavy ion. Since the angular distributions of lighter ejectiles peak at progressively smaller angles, this gives rise

to the asymmetry in the coincident alpha yield. [The relatively small asymmetry observed for the alpha particles in coincidence with oxygen, however, is consistent with the nearly symmetric angular distribution of primary inelastically-scattered neon about $28^{\circ}$. (The primary neon distribution is assumed to be similar to the inclusive distributions.)]

The above considerations demonstrate the consistency of the experimental results with a sequential process. An analysis of the kinetic energies of heavy ion and light fragment will be needed to make stronger statements. However, the distributions in Fig. 3 can, at the very least, be used to demonstrate that the phoswich array is detecting almost all of the alpha particles emitted in coincidence with projectile-like fragments at 11 MeV/nucleon. This high efficiency means that the observation of an ejectile with no accompanying light charged fragment implies that the heavy ion was produced in a charged-particle-bound state. The M=0 portion of the yields in Fig. 2 represents this yield of fragments produced below their charged-particle decay thresholds. The ratios of the M=0 and inclusive yields observed in the present work are listed in Table 2, along with the corresponding ratios taken from the earlier measurements done with the plastic box. For the heaviest fragments, the two sets of data are in good agreement, even though the angle of the detected projectile-like fragment was different ($28^{\circ}$ vs. $15,20^{\circ}$) in the two cases. The ratios for Z=3-6 are larger in the present work than those observed earlier at smaller angles.

III.B. 341 MeV

At the higher bombarding energy, the efficiency for detecting coincident protons and alpha particles is much less than 100%. Unlike the situation at 220 MeV, those ejectiles scattered to the grazing angle have

coincident alpha particles in the vicinity of the beam. Thus, the minimum phoswich angle of ~ $6^{\circ}$ results in a large loss of efficiency. This is illustrated in Fig. 4 by the distributions of coincident alpha particles in the phoswich elements for the configuration with the heavy-ion telescope positioned between segments 2 and 3. Coincidences between heavy ions in the opposite-side telescope and alpha particles in the phoswich array are here displayed as a coincidence between the same-side telescope and a "virtual" phoswich on the opposite side of the beam.

It is clear that the combination of real and virtual light-particle detectors covers only a fraction of the total coincident yield. In fact, the coincident alpha yield appears to peak in the uncovered region. This has two consequences: 1) The total breakup yield can only be estimated, and requires an assumption about the distribution of alpha particles in the uncovered region $-6^{\circ} < \theta < +6^{\circ}$. 2) The array can no longer be used as an event-by-event veto of breakup. Thus, the determination of the charged-particle-bound-state yield performed at 220 MeV cannot be done at 341 MeV.

Attempts were made to estimate the total breakup cross sections by means of a simulation of sequential decay. The relatively strong yield of opposite-side alpha particles in the virtual array could only be reproduced by employing a primary angular distribution that was very strongly forward peaked. It further required that the excitation of the primary fragments be, on average, higher at the more forward angles. However, the simulated yield in the uncovered region near the beam was found to be extremely sensitive to these input distributions, and so a reliable estimate of the missing coincidences could not be made. Although the assumptions made in the simulation regarding primary distributions at 341 MeV are consistent

with results obtained at 220 MeV, the enhancement in opposite-side yield might also be due to non-sequential processes (as will be discussed in the next section on yield reconstructions).

The relative abundance of protons and alpha particles in the region covered by the phoswich arrays still provides much information, in particular about the distribution of excitation energy in the primary projectile-like fragments. Table 1 compares the ratio of the alpha-to-proton yields at 220 and 341 MeV, observed in coincidence with various fragments. The alpha-particle yields dominate the proton yields for all ejectiles except fluorine. This is connected with the low separation energies for alpha-particle emission in most of the primary nuclei produced in these reactions. Generally, the proton threshold lies above the alpha threshold. (In the case of the fluorine channel, the very small cross section for the pickup of a proton by the projectile results in almost no fluorine-alpha coincidences.) At 341 MeV, the relative importance of proton emission has increased such that the alpha-to-proton ratios have decreased from typically 10-20 to 2-4. This indicates that the population distribution of excitation energy in the primary ejectiles has moved upward with increasing bombarding energy, and is in agreement with conclusions obtained from measurements [9] of transfer and breakup cross sections made with the plastic box.

## IV. Yield Reconstructions

The measured coincidence yields correspond to the fraction of the primary yield that decayed via proton or alpha-particle emission. The primary yield is obtained by adding to the coincidence yield the bound (i.e., M=0) yield for the same parent nucleus. The ratio of the bound

yield to the primary yield is called the charged-particle survival fraction of a primary fragment, and represents the probability that the ejectile in a particular primary channel was produced in a state of excitation below its lowest charged-particle decay threshold.

The survival fractions obtained at 220 MeV bombarding energy and at the fragment laboratory scattering angle of 28° are shown in Fig. 5. The survival fractions have been summed over isotope in order to compare with results obtained at 15 and 20° from the plastic box experiment [9]. In general, there is qualitative agreement among the three sets of data. However, there is an apparent trend for the survival fraction to increase with increasing angle of the secondary fragment. (The detection efficiency at 220 MeV was nearly 100%, as was shown in Fig. 3, and thus the change of survival fraction with angle is not due to the smaller solid angle in the present experiment.)

The above results suggest that the excited fragments emitted at angles forward of the grazing angle are, on the average, more highly excited than those scattered to near-grazing angles. This observation is consistent with a process whereby the more inelastic collisions result in scattering to smaller, and then negative, angles under the influence of the nuclear force. In an earlier study at 341 MeV [9], it was observed that the energy spectra of projectile-like fragments emitted forward of the grazing angle had prominent low-energy tails, in contrast to the more-nearly gaussian distributions at the grazing angle. This suggested the presence of deep inelastic processes at very forward angles; the present work supports this suggestion.

It was pointed out in the previous section that simulations of sequential decay at 341 MeV were able to reproduce the observed

alpha/heavy-ion angular correlations (Fig. 4), but only by assuming a strong correlation between primary angle and excitation. In general, the inclusion of forward-peaked distributions with higher excitation at the more forward primary angles would tend to produce forward-angle enhancements of alpha particles in coincidence with a heavy-ion telescope fixed at, e.g., the grazing angle. This is thus an important effect to consider in analyzing measured alpha/heavy-ion correlations, either to demonstrate the consistency of the results with sequential decay [2,3,8] or to try to establish an inconsistency [13].

The charged-particle survival fractions in Fig. 5 refer to a specific laboratory scattering angle for the bound fragment and to a range of primary scattering angles that produce secondary fragments at the indicated laboratory angle. Nevertheless, these differential survival fractions are a useful indicator of the relative breakup probabilities that would be obtained after an integration over scattering angle. Similarly, the charged-particle survival fraction will be a good approximation to the overall survival fraction (i.e., the probability that a primary fragment survives neutron emission as well as charged-particle emission) for those nuclei that have high neutron thresholds. For ejectiles with low neutron thresholds, the overall survival fraction will be less than the charged-particle survival fraction. In these cases, neutron emission must be taken into account.

## V. Kinematic Reconstructions

### V.A. The method

The survival fractions discussed in the previous section provide qualitative information on the excitation produced in primary fragments.

We have also performed [12] a more detailed set of analyses via kinematic reconstructions of the coincidence data [see, e.g., Ref. 14], with attention given to the individual isotopes.

We consider the following process: In the sequential decay of an excited primary (projectile-like) fragment (PF), the excitation is removed (in all or part) by the emission of a photon or, if above threshold, by a particle (typically neutron, proton, or alpha). In the latter case, the secondary projectile-like fragment (PLF) and emitted light fragment (LF) emerge with a relative velocity characterizing the decay. The excitation in the PF and PLF are related by

$$E_x(PF) = E_x(PLF) + E_{rel} + S \ ,$$

where $E_{rel}$ is the relative kinetic energy of the PLF and LF, and S is the associated separation energy. For particle decay to the ground state of the PLF, the excitation-energy distribution in the primary ejectile is then completely determined by the energies and positions of the detected secondary fragments.

The detection of the PLF and LF leaves only the target-like fragment (TLF) undetected. By employing conservation of energy:

$$T_{PLF} + T_{LF} + T_{TLF} + Q_3 = T_{beam}$$

and conservation of linear momentum:

$$P_{PLF} + P_{LF} + P_{TLF} = P_{beam}$$

it is possible to calculate the kinetic energy of the unobserved target recoil and, thus, the three-body Q-value, $Q_3$. Finally, the excitation in the TLF is calculated from the relation

$$E_x(TLF) = Q_{ggg} - Q_3 \ ,$$

where $Q_{ggg}$ is the ground-state Q-value calculated from the difference between the entrance- and exit-channel masses of the nuclei in their ground states.

The above prescription means that, from event-by-event coincidence data, it is possible to construct the excitations in the two primary fragments by studying the decay of one of these two nuclei. The reconstruction of the PF excitation makes the assumption: (1) the emitted LF resulted from the sequential decay of the PF. Both PF and TLF excitation reconstructions also assume: (2) the secondary fragments that are detected (i.e., PLF and LF) were produced in their respective ground states, and (3) the only additional (undetected) particles are the TLF and its decay products. The validity of these assumptions can be tested from the reconstructed data.

Assumption (1) has been borne out by many studies in this energy regime [2-8]. The dominance of sequential breakup (as compared to a prompt mechanism) can also be seen in the present set of data by examining the position and energy correlations of the coincident fragments. The two-dimensional distribution (x-y) of alpha particles in the phoswich array is shown in Fig. 6 for those alpha particles detected in coincidence with $^{16}O$ ejectiles produced in the reaction at 220 MeV. (The horizontal-position information is limited to knowing which segment detected the alpha particle, but in Fig. 6 this discrete information is randomized across the width of the segment.) As can be seen, there is an enhancement of yield in close proximity to the position of the trigger telescope.

More information can be obtained by plotting the energy-position distribution of the alpha particles in each segment. This is shown in Fig. 7 as a plot of the laboratory kinetic energy vs. vertical position of the

coincident alpha particles for each of the eight phoswich segments. There is an obvious correlation in these plots which can be identified as arising from sequential decay of an excited $^{20}Ne$ projectile.

The kinematics associated with breakup reactions is illustrated by the schematic diagram in Fig. 8. In this example, the sphere is generated by a single value of the relative kinetic energy. For the segments closest to the heavy-ion telescope, the energy of the detected alpha particle will depend strongly on position. The alpha particles in the middle of the segment (and thus closest to the telescope) correspond to breakup reactions in which the secondary fragments are colinear with the primary fragment momentum. Therefore, the alpha energies will be double valued, and the energy will depend on whether the emission was parallel or anti-parallel to the primary trajectory. The alpha particles closer to the edges of segments 4 and 5, on the other hand, correspond to breakup perpendicular to the primary momentum vector, resulting in energies that are beam-like (for both alpha and PLF). The kinematics of the breakup process will thus give rise to a ring-like structure. The two rings in segments 4 and 5 of Fig. 7 represent the population and decay of several states in primary $^{20}Ne$. The inner ring corresponds to decay from states at 5.6 and 5.8 MeV. The outer ring is built up from a cluster of states around 7 MeV. (The energy and position resolution of the phoswich array does not permit resolution of these individual states.)

In contrast, the energies of the particles observed in segments 3 and 6 are more characteristic of the beam velocity, and they are concentrated towards the center of the segments. This is even more apparent in segments 2 and 7. For these segments, the coincidences arise

from the perpendicular (rather than colinear) breakup configuration. This corresponds to sampling the side caps of the breakup sphere.

Segments 4 and 5 of Fig. 7 also show a depletion of yield for alpha particles detected in the middle of the segment. There is, of course, some shadowing of the center of the inner-most segments by the heavy-ion telescope. However, as can be seen in this representation, this loss constitutes a small fraction of the breakup yield in those segments. Thus, the local minima in yield observed for segments 4 and 5 in Fig. 3 is probably due to kinematics rather than detector efficiency: a concentration of alpha emission in the reaction plane due to transferred angular momentum would tend to produce a dip for the segments closest to the detected heavy ion. (Such a kinematical effect has been observed in simulations of sequential breakup.)

At the higher bombarding energy of 341 MeV, the individual laboratory kinetic energies of coincident alpha particles and $^{16}O$ ejectiles [Fig. 9] are peaked at the beam velocity. Rather than plot the energy vs. position of the coincident alpha particle, it is useful to construct the relative-velocity vector since this preserves the correlation information even when the primary fragment has a distribution of velocities. This relative-velocity vector is represented in Fig. 10 as a decomposition into components perpendicular to and parallel to segment 2, for those alpha particles detected in segment 2. (Note that at 341 MeV, the heavy-ion telescope was positioned between segments 2 and 3.) This "slice" through the middle of the breakup sphere shows essentially the same features seen in Fig. 7, i.e., rings associated with states in primary $^{20}Ne$. Once again, we have a yield dominated by a sequential mechanism.

In addition to inelastic breakup of the projectile, such correlations are also observed (at both 220 and 341 MeV) for coincident data corresponding to primary transfer processes, and thus assumption (1) [sequential decay of the PF] is a proper one in the kinematic reconstruction. Assumptions (2) [secondary fragments in ground states] and (3) [no undetected fragments] will be shown to be approximately valid in the next section on reconstructed PF excitations.

The use of a large-solid-angle array for the detection of light charged particles also enables the study of relatively weak exit channels. This is illustrated in Fig. 11, which shows the energy spectra of $^{20}$Ne in coincidence with protons. The large elastic peak corresponds to random coincidences. However, the structure at lower energies arises from true $^{20}$Ne + p coincidences, and thus corresponds to the decay of $^{21}$Na following one-proton pickup.

V.B. Reconstructed PF excitations at 220 MeV

A spectrum of relative kinetic energy is shown in Fig. 12 for the $^{12}$C + $\alpha$ channel (primary $^{16}$O). The shifting of the energy axis by the appropriate separation energy will, subject to assumptions about the decay process, yield a spectrum of excitation in the primary ejectile. Many of the features of this spectrum are common to the other reconstructed channels and, thus, bear comment. The spectral distribution is identically zero for energies below the alpha threshold at 7.16 MeV. The excitation distribution then quickly climbs, peaking at ~ 9½ MeV, and then drops exponentially.

These features are strongly influenced by the structure of $^{16}$O, since the first alpha-decaying state is the $1^-$ at 9.63 MeV (i.e., 2.47 MeV

above the threshold for decay). This state coincides with the position of the peak in the reconstructed spectrum. For a sequential process, the region between threshold and 9.63 MeV is forbidden. (The 8.87-MeV $2^-$ state has a negligible branching ratio for alpha decay.) The tail of the distribution that occupies this region thus represents the resolution of the reconstruction technique, with the main contributions coming from the energy and position resolutions of the phoswich array. The exponential reduction in population at higher excitations indicates that the intrinsic distribution of excitations in primary $^{16}O$ is peaked at some value below threshold.

The primary $^{16}O$ channel can now be used to test the two remaining assumptions in the kinematic reconstructions. The exponential drop in excitation above the first alpha-decaying state means that there is relatively little feeding of the 4.4-MeV first excited state in the $^{12}C$ PLF, since such feeding must come from primary excitations in excess of 11.6 MeV. Thus, assumption (2) [both detected fragments in ground states] is usually satisfied in this case, and, in general, is true for the stripping products.

The third assumption of the reconstruction is that the decay of the primary fragment produces only two bodies. Since the phoswich array has a high efficiency for detecting coincident light charged fragments, and since the yield of M=2 events was negligible, any additional undetected fragment must be a neutron. For the specific case of the $^{12}C + \alpha$ channel, this would correspond to the decay of primary $^{17}O$, via $\alpha n$ (or $n\alpha$) emission.

This primary fragment ($^{17}O$) can be studied via $^{13}C + \alpha$ coincidences, and this excitation spectrum is plotted in Fig. 13. The reconstructed distribution has almost no yield above 14 MeV. Since the

branching ratio for alpha decay to the ground state is still significant at this excitation, this shows that such large excitations in primary $^{17}O$ are very weakly populated. Therefore, the emission of an alpha particle and neutron (for which 14 MeV is the effective threshold) is not significant. In this case, which is typical for this bombarding energy, the application of three-body kinematics [assumption (3)] to the charged-particle coincidence data is valid.

Due to the low neutron-decay threshold in $^{17}O$, there exists a region of primary excitation from 4.1 to 6.4 MeV in which neutron decay is the only particle-emission channel. The spectrum for primary $^{17}O$ (Fig. 13) does not contain this important neutron channel. This band of excitation is of unknown strength, and will contribute to the apparent yield of M=0 $^{16}O$. This would thus constitute a contribution to the two-body events by three-body processes, and would modify the apparent charged-particle survival fractions. Because of the large primary $^{16}O$ cross section, such a "contamination" is not very important, though this may not be true for all primary ejectiles.

By comparison, the contamination of the three-body data by four-body processes is much weaker (as deduced by three-body reconstructions and charged-particle multiplicities), indicating the utility of using the coincidence data for examining primary excitations in this energy regime.

The $\alpha$-particle coincidence data were used to reconstruct the excitations in eight primary ejectiles (shown in Fig. 14). In Figs. 12, 13, and 14 the yield of particle-bound primary ejectiles (corresponding to M=0 events) is represented by the hatched regions below the alpha threshold. For all channels, the bound-state (two-body) yields are larger than the alpha-decay yields. This result is consistent with primary

ejectiles being produced, on average, at below-threshold excitations. However, the channels with low neutron thresholds (i.e., $^{17,18}O$, $^{21,22}Ne$) will have regions of excitation below (and, to a lesser extent, above) the first charged-particle threshold that decay by emitting a neutron.

For those events in which the heavy-ion telescope is triggered by a projectile-like fragment, the efficiency for detecting a sequentially-emitted proton or alpha particle is dependent on $E_{rel}$ . This efficiency will obviously become smaller when the breakup sphere is larger than the array, i.e., for very large relative energies. While the phoswich array was observed to cover most of the angular distribution associated with alpha emission (see Figs. 3 and 7), the dependence of efficiency upon relative energy may strongly distort some features of the $E_{rel}$ spectrum.

To study this, the efficiency, $\epsilon(E_{rel})$, has been determined by performing Monte Carlo simulations of sequential decay. (The alpha decay is assumed to be isotropic in this calculation.) The results of these simulations are presented in Fig. 12 for the primary alpha-transfer channel leading to $^{12}C + \alpha$ coincidences. For very small relative energies the alpha-particle efficiency suffers from shadowing by the heavy-ion telescope, but, due to the compact geometry of the telescope, shadowing effects are no longer important for $E_{rel} > 400$ keV. The efficiency is then almost constant up to $E_{rel} \approx 5.2$ MeV, at which point the breakup sphere's dimensions exceed those of the phoswich array and, as a result, the detection efficiency falls. The influence of the primary angular distribution upon this efficiency profile is, of course, an important consideration. Simulations were performed using both an isotropic and a strongly forward-peaked primary distribution, and the resulting efficiency curves were essentially identical. Therefore, while primary angular

distributions must be carefully considered when analyzing coincidence data with typical experimental configurations, the use of a large-solid-angle system like the phoswich array makes such considerations less critical.

A comparison with the exponentially falling distribution of excitation in primary $^{16}O$ shows that the efficiency of the phoswich array will not appreciably modify the $E_{rel}$ spectrum. In fact, returning to Fig. 14, the yields of almost all primary channels have dropped considerably for $E_{rel} > 5.2$ MeV. Therefore, with the exception of primary $^{22}Ne$, the reconstructed PF excitations will not be changed appreciably by an efficiency correction.

The $E_x(PF)$ distributions will also be modified by competition with other decay modes. For example, the low proton-decay threshold in primary $^{18}F$ means that proton emission will sample part of the total primary excitation distribution. However, the $^{14}N + \alpha$ yield was $\sim 2\frac{1}{2}$ times the $^{17}O + p$ yield, showing that the alpha channel is the dominant decay mode of primary $^{18}F$. Therefore, any modification of the spectral shape is restricted to the tail of the distribution.

The situation is less clear for primary $^{17,18}O$ and $^{21,22}Ne$, where the importance of neutron decay cannot be assessed experimentally. It thus becomes necessary to perform statistical-model calculations to account for the neutron competition. This has been done using the statistical-model code STATIS [15], with transmission coefficients generated from optical-model calculations. The results of such calculations for primary $^{22}Ne$ are shown in Fig. 15, where the branching ratios for alpha and neutron decay, $\Gamma_\alpha/\Gamma_{total}$ and $\Gamma_n/\Gamma_{total}$, are plotted as a function of primary excitation energy. These calculations show that neutron decay dominates by an order of magnitude at excitations several MeV above the alpha threshold, with

neutron emission becoming still more favored at near-threshold excitations because of the Coulomb barrier associated with alpha emission. Thus, without a correction for neutron emission, the excitations reconstructed from $^{18}O + \alpha$ coincidences are not a true representation of the total primary excitation distribution, in either yield or spectral shape.

V.C. Reconstructed TLF excitations at 220 MeV

The primary excitations in the target-like fragment were reconstructed event-by-event, subject to assumptions already discussed. These reconstructed excitations are shown in Fig. 16 for the same coincidence channels considered in Fig. 14. In this case, the threshold for particle decay of the primary ejectile does not limit the accessible region of excitation in the TLF.

However, it is still possible that the coincidence requirement imposes a bias on the reconstructed TLF excitations. Consider the following two scenarios: (1) The total primary excitation, $E_x(PF+TLF)$, is constant. In this case, the requirement that the PF be excited above threshold will select a subset of TLF excitations that are smaller than the mean. (2) The ratio of excitations, $E_x(PF)/E_x(TLF)$, is constant. In this case, the subset of TLF excitations being examined via the coincidence data is higher than the mean.

To ascertain the effects of a possible bias, the event-by-event reconstructions were used to generate contour plots of $E_x(PF)$ vs. $E_x(TLF)$. These plots are shown in Fig. 17 for the primary $^{22}Ne$ and $^{18}F$ channels. Fig. 17 shows no apparent dependence of the TLF excitation on PF excitation for the pn-stripping and 2n-pickup channels. Specifically, the average TLF excitations are unchanged when gated by different PF-excitation bins.

Furthermore, there is no indication from the observations above threshold that the average TLF excitations are changing as the PF excitations go sub-threshold. Based on this, we conclude that there are no strong biases on TLF excitation imposed by the experimental technique.

V.D. Reconstructed excitations at 341 MeV

The kinematic analysis at 341 MeV proceeds in the same manner as for 220 MeV. The similarities in the results are perhaps more striking than the differences. The PF and TLF excitations at 220 and 341 MeV are compared in Figs. 18 and 19 for the primary $^{16}O^*$ channel. The PF (Fig. 18) is observed to peak at the same $E_{rel}$ at both bombarding energies. An exponential drop in yield at higher excitations is also common to both spectra. However, the 341-MeV distribution falls more gradually than does the one at 220 MeV. It is thus clear that a higher bombarding energy produces a distribution of excitation energies for the PF that is higher, even for stripping reactions. This is also borne out by the plastic box work, which deduced lower survival fractions at 341 MeV than at 220 MeV.

The TLF excitations (Fig. 19), however, show a much stronger dependence on bombarding energy for the $\alpha$-stripping channel. The capture of an alpha particle at 341 MeV results in the population of much higher excitations in the target-like fragment than was achieved at 220 MeV. Thus, in addition to the excitation depending on the mass transferred (as seen in Fig. 16), there is an obvious dependence on bombarding energy, at least for the nucleus acquiring mass.

## VI. Discussion

The reconstructed TLF excitations at 220 MeV, plotted in Fig. 16, can be used to ascertain the amount of excitation generated in the target as a function of mass transfer (or channel). To help interpret these results, it is instructive to extract the most-probable, or peak, value from the excitation distributions. These most-probable excitations, at both 220 and 341 MeV, are plotted in Fig. 20 for various channels (denoted by the associated PF). While the magnitude of the excitations is greater at the higher bombarding energy, the trends in the data are the same: the target-like fragment acquires more excitation when it acquires more mass.

For the purposes of making quantitative arguments, we discuss the 220-MeV data for four particular channels: primary $^{16}O$, $^{18}F$, $^{20}Ne$, and $^{22}Ne$. These primary channels correspond to $\alpha$ stripping, pn stripping, inelastic scattering, and 2n pickup, respectively.

The reconstructed PF excitations for these four channels are shown in Fig. 21 (note the linear scale). Also indicated in the figure is the position of the lowest alpha-decaying state (or cluster of states) for each of the primary projectile-like fragments. For the stripping and inelastic channels, the reconstructed PF excitations peak at these lowest decaying states, and drop exponentially towards higher excitations. These distributions are consistent with a primary distribution that is peaked at excitations below the alpha-decay threshold.

Such an inference is, in turn, corroborated by the breakup probabilities for the primary fragments. More than 96% of the primary $^{16}O$ yield populated states below the decay threshold of 7.2 MeV, indicating that the average excitation of primary $^{16}O$ is much smaller than 7.2 MeV. Similarly, the survival fractions of $^{18}F$ and $^{20}Ne$ are far in excess of 50%,

indicating that these primary fragments are also being created cold (relative to their decay thresholds).

In the case of two-neutron pickup (primary $^{22}$Ne), the reconstructed excitations are populating excitations that are several MeV beyond the lowest alpha-decaying states. The interpretation of this is complicated, however, by the presence of a low neutron-decay threshold in $^{22}$Ne, which results in strong competition between neutron and alpha emission. In principle, the neutron and alpha branching ratios calculated with the statistical-model code STATIS (Fig. 15) may be used to correct the reconstructed excitation in Fig. 21(d). However, the large variation in transmission coefficients in the near-to-threshold region makes the calculation of $\Gamma_\alpha/\Gamma_n$ subject to uncertainty.

A more reliable approach is to work only with that portion of the $^{18}$O + $\alpha$ yield arising from excitations in excess of 11.5 MeV, for which the optical-model-generated transmission coefficients are more certain. In this case, even excluding the lowest excitations, the predicted neutron yield is much larger than the alpha yield. After correcting for this unobserved neutron yield, the charged-particle survival fraction of primary $^{22}$Ne is $\approx$ 35%, which demonstrates that the $^{22}$Ne ejectiles are produced with average excitations greater than the 9.7-MeV alpha-decay threshold. This is in sharp contrast to the channels shown in Fig. 21(a,b,c), for which small excitations were deduced. However, it is consistent with the results of Siwek-Wilczynska et al. [16], in which particle-gamma coincidences indicated that pickup reactions resulted in highly excited projectile-like fragments.

In Fig. 22, the reconstructed TLF excitations, deduced from three-body kinematics, are shown for the same four channels already considered in

Fig. 21. The excitation acquired by the target-like fragment is correlated with the amounts of mass and charge transferred to the target. This effect is well-known from near-barrier transfer studies, and has been successfully reproduced with optimum-Q-value calculations that provide Coulomb-corrected Q-values.

Such a calculation was outlined by Siemens et al. [17], for predicting the most-probable Q-values associated with few-nucleon transfer reactions. The fundamental assumption of this optimum-Q-value model is that, on the average, the transferred nucleons are at rest with respect to the donor nucleus (or nuclei, for bi-directional transfer). The calculation can be performed using simple kinematics to account for recoil effects. The energetics of the transfer process then yields the expression for the optimum Q-value. In the Siemens prescription, the optimum Q-value for a reaction A(a,b)B can be written in the following simplified form [18]:

$$Q_{opt} = V_C(out) - V_C(in) - \frac{E_{cm} - V_C(in)}{\mu_{in}} \left[ n \frac{A-m}{B} + m \frac{a-n}{b} \right]$$

where n nucleons are transferred from projectile to target and m nucleons from target to projectile. Here, $\mu_{in}$ is the entrance-channel reduced mass. The exit- and entrance-channel Coulomb potentials at contact, $V_C(out)$ and $V_C(in)$, are evaluated using a radius parameter $r_C = 1.4$ fm. The total excitation energy is then given by

$$E_x(total) = Q_{gg} - Q_{opt} \ .$$

This calculated total <u>available</u> excitation energy is indicated in Fig. 22 (arrows). The TLF excitations for the stripping and inelastic channels account for almost all of this available excitation. By contrast, the target-like fragment produced in two-neutron pickup acquires a small

portion of the total excitation energy. (Conversely, recall that the primary $^{22}$Ne ejectiles were produced at relatively high excitations.)

These results clearly show that nucleon transfer is the most important mechanism for generating excitation energy in the peripheral reactions studied in the present work. Moreover, the division of excitation energy between the projectile-like and target-like fragments indicates that the partition of excitation is governed by the direction of the mass transfer. To first approximation, the fragment that is donating mass remains cold while the recipient nucleus acquires excitation. The short interaction times associated with these peripheral reactions cause the observed division of excitation to be frozen at this mass-transfer partition. Unlike the more highly damped reactions studied with heavier projectiles [19-23], there is apparently not enough time for a redistribution of the excitation energy (e.g., towards thermalization). Thus, the data presented in this work represent reaction mechanisms at the earliest stages of the dissipation process.

It is interesting to consider the above results in light of the observation of non-equilibrium excitation-energy sharing in partially-damped reactions of heavier projectiles [24,25]. The almost-equal partitions observed in these recent studies are predicted by transport-model calculations of nucleon exchange [26], and arise from the equal flux of nucleons to and from the projectile at the initial stage of the reaction. The present work, which focuses on excitation partition as a function of mass transfer rather than Q-value, shows unambiguously that nucleon exchange is responsible for the generation and partition of excitation energy. While the collision geometry and interaction time of the reactions studied in the present work tend to suppress transport

processes [27], it nevertheless provides support for the underlying ansatz of the transport model. Similar results have been reported for the partition of excitation in few-nucleon transfer reactions induced by much heavier projectiles [28].

The strong correlation between mass transfer and excitation generation suggests that the Siemens optimum-Q-value model, which was used to predict most-probable total excitations, may be extended to predict the primary excitations in each of the outgoing fragments as well. We have made this extension by employing the following ansatz: the primary fragments acquire a fraction of the total available excitation energy in proportion to the number of nucleons captured. Such a captured-mass-ratio sharing leads to the following relations:

$$E_x(\mathrm{PF}) = \frac{m}{m+n} E_x(\mathrm{total}) \ , \quad \text{and}$$
$$E_x(\mathrm{TLF}) = \frac{n}{m+n} E_x(\mathrm{total}) \ .$$

Here, the total excitation is deduced from $Q_{opt}$, with m and n denoting the nucleons transferred in both directions.

The results of such calculations are shown in Fig. 23, for the most-probable TLF excitations measured at 220 MeV bombarding energy. While the model deals with the total, or gross number of transferred nucleons, the experimental yields are in terms of the net transfer of mass. However, since the interaction times are relatively short, a first approximation is to assume that the net and gross transfers are one and the same. This then leads to the calculated most-probable TLF excitations, indicated by the open circles in Fig. 23. For the inelastic and pickup channels, zero excitation is, of course, a trivial result; however, it is also in general agreement with the reconstructed excitations. Good agreement is also obtained for $^{18,19}F$ and, in particular, $^{16}O$.

The discrepancy between calculation and experiment for $^{17,18}O$, however, is serious enough to suggest that another mechanism is generating the observed excitations. Such a mechanism might be a complex (bi-directional) mass flow, in which an alpha particle is transferred to the target, along with one- and two-neutron pickup to the projectile for $^{17}O$ and $^{18}O$, respectively. If such a process is used in the calculation of target excitation (open squares), agreement is obtained.

The use of a complex process for the primary $^{17,18}O$ channels is physically meaningful. It has been noted by Homeyer et al. [29] that the experimental ejectile yields can be predicted by a cluster-stripping model if the stripping is accompanied by a strong neutron-pickup mechanism. For alpha-cluster nuclei such as $^{20}Ne$, the alpha-stripping cross section is demonstrably large. Furthermore, the neutron-pickup cross section is known to be quite large when neutron-excess targets are used. Therefore, the importance of bi-directional transfer in the production of primary $^{17,18}O$ may be comparable to the uni-directional component. It should be emphasized that the coincidence data used in the present work examines that subset of the primary yield resulting in ejectiles excited above threshold. Thus, the coincidence data might be expected to be more sensitive to the bi-directional component of the $^{17,18}O$ yield.

A similar analysis of TLF excitations has been performed at 341 MeV, and is shown in Fig. 24. In general, the agreement is not as good as at the lower bombarding energy. In particular, there are large discrepancies between calculated and reconstructed TLF excitations for the primary $^{22}Ne$ and $^{16,17,18}O$ channels. For $^{17,18}O$, this discrepancy is not removed by a bi-directional calculation.

The apparently large TLF excitation at 341 MeV for two-neutron pickup to the projectile may represent the breakdown of the assumption that sequential decay leaves the PLF in its ground state. For $^{22}$Ne, the survival fraction at 220 MeV indicated that large excitations were populated in the PF. Such excitations ought to be even larger at the higher bombarding energy, at which point alpha decays to excited states in $^{18}$O would have large branching ratios. An excited $^{18}$O PLF would cause the kinematic reconstructions to underestimate the excitation in primary $^{22}$Ne. Conversely, the reconstructed TLF excitation would be enhanced.

The primary $^{17,18}$O channels suggest that the bi-directional transfer is not properly treated. The simple calculations performed for bi-directional channels are consistent with a cold donor nucleus; however, other algorithms consistent with this could be tried. For example, the bi-directional transfer could be treated by two separate uni-directional calculations, with the recipient nucleus acquiring the full excitation of each step. Unfortunately, the time ordering of the steps (e.g., $\alpha$n or n$\alpha$) must be specified, since different excitations are obtained. In practice, however, either ordering gives roughly the same excitations as derived from the "simultaneous" process already considered.

The results at 341 MeV for primary oxygen may be interpreted two ways. One possibility is that the target-like fragments associated with primary oxygen are acquiring additional excitation through a process not incorporated in the simple Q-value calculations, such as collective excitations. Another possibility is that the exit channels are no longer three-body but that an additional, undetected particle from the projectile-like fragment is present, causing the three-body kinematics to reconstruct erroneously large TLF excitations. The latter case could correspond to the

presence of non-statistical (or non-equilibrium) neutrons in the transfer channels. In this case, the results of Petit et al. [30] on neutron emission are relevant. For reactions leading to projectile-like fragments, no non-equilibrium neutrons were observed for reactions induced by 9- or 12-MeV/nucleon $^{20}Ne$ beams. However, a non-statistical yield was observed with 16-MeV/nucleon $^{12}C$ beams. Therefore, fast neutrons might be the cause of the anomaly observed in the present work at 17 MeV/nucleon.

If neutrons are emitted at the time of contact and with the velocity of the projectile at contact, the fast neutrons should have about 12 MeV of kinetic energy. Therefore, the presence of an additional neutron in the primary $^{16,17,18}O$ channels would remove the existing discrepancies between calculated and reconstructed excitations. More experiments will have to be performed before this interpretation can be properly tested. However, it suggests that the present experimental technique used to determine primary excitation may be limited to bombarding energies not greatly in excess of 11 MeV/nucleon.

## VII. Summary and Conclusions

Breakup reactions induced by inelastic scattering and nucleon transfer have been studied by performing coincidence measurements between projectile-like fragments and light charged fragments (protons or alpha particles). The $^{20}Ne$ + $^{197}Au$ system was examined at $^{20}Ne$ bombarding energies of 220 and 341 MeV (11 and 17 MeV/nucleon).

Projectile-like fragments were detected in a small-solid-angle telescope positioned slightly forward of the classical grazing angles of the two bombarding energies. Light fragments were registered in a large-solid-angle phoswich array [10,11], which provided position, energy, and

multiplicity information. At 220 MeV, the very high efficiency for observing sequentially-emitted light fragments made it possible to measure the yield of primary fragments produced in charged-particle-bound states.

At both bombarding energies, the multiplicity of light charged particles associated with sequential ejectile decay was low: usually no more than one proton or alpha particle in coincidence with fragments lighter than the beam. This result is in agreement with earlier $4\pi$ measurements [9]. In turn, the coincidence yield is dominated by alpha particles, which suggests relatively low primary excitations. At 341 MeV, however, proton decay becomes relatively more important, indicating that ejectile excitations are correspondingly higher. There are also indications at 220 MeV that projectile-like fragments emitted near the grazing angle are cooler than fragments emitted at more forward angles. In general, however, reconstructed yields show that transfer of mass to the target results in primary projectile-like fragments that are usually excited below the particle-decay threshold.

The coincidence data were also used to make kinematic reconstructions of specific transfer channels corresponding to few-nucleon stripping and pickup, as well as inelastic scattering. These kinematic reconstructions of excitations in the primary projectile-like and target-like fragments assumed the sequential decay of an excited projectile-like fragment, resulting in a three-body channel with both detected fragments left in their ground states. Reconstructed excitations indicated that these assumptions were, on average, satisfied.

At 220 MeV, the deduced breakup probabilities were very low for stripping and inelastic channels. These results were supported by the excitation distributions, which were peaked at the lowest particle-decaying

state, in accord with small average excitations. However, the pickup channels (e.g., $^{22}$Ne) had much larger breakup probabilities and indicated highly excited primary fragments. The target-like fragments showed a complimentary behavior. The stripping channels resulted in large target excitations, while the pickup reactions produced relatively cold target recoils.

Quantitative comparisons were made with excitations predicted by the optimum-Q-value model of Siemens et al. [17]. For stripping channels, the most-probable target-like excitations were well-reproduced by the calculation, indicating that the target recoil was acquiring essentially all of the available excitation (in accord with the low ejectile excitations observed). On the other hand, the target-like fragments associated with projectile pickup were much colder than the predicted total excitations, with the balance of the excitation apparently going into the projectile-like fragment, again in accord with the high excitations observed for the pickup products.

Such results demonstrated that, in these peripheral collisions, the excitation is generated by the transfer of nucleons and, moreover, the partition is governed by the direction of the mass flow. This observed partition suggested an extension of the Siemens optimum-Q-value model, whereby the excitation of each of the primary fragments may be predicted using the ansatz that the $Q_{opt}$-predicted total excitation is shared in the ratio of the captured mass. This algorithm predicted primary excitations in qualitative and quantitative agreement with the reconstructed projectile-like and target-like excitations, respectively. A discrepancy for the primary $^{17}$O and $^{18}$O channels could be removed only by employing a bi-directional transfer process in the Q-value calculation. This is

believed to signify the importance of neutron pickup in alpha-stripping reactions, and suggests that breakup studies are particularly sensitive to the bi-directional component in transfer yields.

A similar analysis of primary excitations could be made at 341 MeV, even though the phoswich array missed a portion of the breakup sphere. The target-like fragments showed the same trends observed at 220 MeV: large excitations when mass was captured, and small excitations when mass was lost to the projectile. The agreement between observed excitations and predicted excitations was not as good as at the lower bombarding energy, with the oxygen isotopes having higher apparent excitations than predicted by the extended Siemens model. This discrepancy might be due to the presence of pre-equilibrium neutrons, or the statistical emission of neutrons by the primary or secondary projectile-like fragment, which would invalidate the use of three-body kinematics in the analysis. An extension of the present study to higher bombarding energies, while of great physical interest, may thus suffer from an extensive contamination of the three-body events by four-body final states.

## Acknowledgments

The authors would like to thank Drs. K. Siwek-Wilczynska and J. Wilczynski for many fruitful discussions. One of us (E.C.) would like to acknowledge the partial support of CONACYT Mexico, under contract PPCCBBNA-022683. This work was supported by the Director, Office of Energy Research, Division of Nuclear Physics of the Office of High Energy and Nuclear Physics, and by the Nuclear Sciences of Basic Energy Sciences Program of the U.S. Department of Energy under Contract DE-AC03-76SF00098.

## References

(a) Present address: Department of Physics and Astronomy, University of Rochester, Rochester, New York 14627

(b) Present address: Gesellschaft fur Schwerionenforschung, Darmstadt, West Germany

(c) Present address: Instituto de Fisica, Universidad Nacional Autonoma de Mexico, Mexico, D.F.

(d) On leave from the Fysisch Laboratorium, University of Utrecht, Utrecht, The Netherlands.

[1] H.C. Britt and A.R. Quinton, Phys. Rev. 124, 877 (1961).

[2] M. Bini, C.K. Gelbke, D.K. Scott, T.J.M. Symons, P. Doll, D.L. Hendrie, J.L. Laville, J. Mahoney, M.C. Mermaz, C. Olmer, K. Van Bibber, and H.H. Wieman, Phys. Rev. C 22, 1945 (1980).

[3] G.R. Young, R.L. Ferguson, A. Gavron, D.C. Hensley, F.E. Obenshain, F. Plasil, A.H. Snell, M.P. Webb, C.F. Maguire, and G.A. Petitt, Phys. Rev. Lett. 45, 1389 (1980).

[4] A. Gamp, M. Burgel, M.R. Clover, C. Egelhaaf, H. Fuchs, B. Gebauer, H. Homeyer, and J.C. Jacmart, Z. Phys. A 300, 63 (1981).

[5] S. Wald, I. Tserruya, Z. Fraenkel, G. Doukellis, H. Gemmeke, and H.L. Harney, Phys. Rev. C 25, 1118 (1982).

[6] H. Homeyer, M. Burgel, M. Clover, Ch. Egelhaaf, H. Fuchs, A. Gamp, D. Kovar, and W. Rauch, Phys. Rev. C 26, 1335 (1982).

[7] P.B. Goldhoorn, G.J. Balster, H.J. Koeslag, R.J. de Meijer, R.H. Siemssen, Z. Sujkowski, and H.W. Wilschut, Phys. Lett. 142B, 14 (1984).

[8] C.P.M. van Engelen, E.A. Bakkum, R.J. Meijer, and R. Kamermans, Phys. Rev. C 33, 1851 (1986).

[9] S. Wald, S.B. Gazes, C.R. Albiston, Y. Chan, B.G. Harvey, M.J. Murphy, I. Tserruya, R.G. Stokstad, P.J. Countryman, K. Van Bibber, and H. Homeyer, Phys. Rev. C 32, 894 (1985).

[10] M. Bantel, R.G. Stokstad, Y.D. Chan, S. Wald, and P.J. Countryman, Nucl. Instrum. Methods 226, 394 (1984).

[11] H.R. Schmidt, M. Bantel, Y. Chan, S.B. Gazes, S. Wald, and R.G. Stokstad, Nucl. Instrum. Methods A242, 111 (1985).

[12] H.R. Schmidt, S.B. Gazes, Y. Chan, R. Kamermans, and R.G. Stokstad, Phys. Lett. 180B, 9 (1986).

[13] R.K. Bhowmik, J. Van Driel, R.H. Siemssen, G.J. Balster, P.B. Goldhoorn, S. Gonggrijp, Y. Iwasaki, R.V.F. Janssens, H. Sakai, K. Siwek-Wilczynska, W.A. Sterrenburg, and J. Wilczynski, Nucl. Phys. A390, 117 (1982).

[14] W.D.M. Rae, A.J. Cole, B.G. Harvey, and R.G. Stokstad, Phys. Rev. C 30, 158 (1984).

[15] R.G. Stokstad, Yale University report WNSL 52 (1972).

[16] K. Siwek-Wilczynska, R.A. Blue, L.H. Harwood, R.M. Ronningen, H. Utsunomiya, J. Wilczynski, and D.J. Morrissey, Phys. Rev. C 32, 1450 (1985).

[17] P.J. Siemens, J.P. Bondorf, D.H.E. Gross, and F. Dickmann, Phys. Lett. 36B, 24 (1971).

[18] J. Wilczynski, Proc. Int. Conf. Nucl. Phys. - Florence, II, 305 (1983).

[19] F. Plasil, R.L. Ferguson, H.C. Britt, R.H. Stokes, B.H. Erkkila, P.D. Goldstone, M. Blann, and H.H. Gutbrod, Phys. Rev. Lett. 40, 1164 (1978).

[20] B. Tamain, R. Chechik, H. Fuchs, F. Hanappe, M. Morjean, C. Ngo, J. Peter, M. Dakowski, B. Lucas, C. Mazur, M. Ribrag, and C. Signarbieux, Nucl. Phys. A330, 253 (1979).

[21] Y. Eyal, A. Gavron, I. Tserruya, Z. Fraenkel, Y. Eisen, S. Wald, R. Bass, C.R. Gould, G. Kreyling, R. Renfordt, K. Stelzer, R. Zitzmann, A. Gobbi, U. Lynen, H. Stelzer, I. Rode, and R. Bock, Phys. Rev. Lett. 41, 625 (1978).

[22] D. Hilscher, J.R. Birkelund, A.D. Hoover, W.U. Schroder, W.W. Wilcke, J.R. Huizenga, A. Mignerey, K.L. Wolf, H.F. Breuer, and V.E. Viola, Jr., Phys. Rev. C 20, 576 (1979).

[23] I. Tserruya, A. Breskin, R. Chechik, Z. Fraenkel, S. Wald, N. Zwang, R. Bock, M. Dakowski, A. Gobbi, H. Sann, R. Bass, G. Kreyling, R. Renfordt, K. Stelzer, and U. Arlt, Phys. Rev. C 26, 2509 (1982).

[24] R. Vandenbosch, A. Lazzarini, D. Leach, D.-K. Lock, A. Ray, and A. Seamster, Phys. Rev. Lett. 52, 1964 (1984).

[25] T.C. Awes, R.L. Ferguson, R. Novotny, F.E. Obenshain, F. Plasil, S. Pontoppidan, V. Rauch, G.R. Young, and H. Sann, Phys. Rev. Lett. 52, 251 (1984).

[26] J. Randrup, Nucl. Phys. A327, 490 (1979).

[27] J. Randrup, Nucl. Phys. A452, 105 (1986).

[28] H. Sohlbach, H. Freiesleben, P. Braun-Munzinger, W.F.W. Schneider, D. Schull, B. Kohlmeyer, M. Marinescu, and F. Puhlhofer, Phys. Lett. 153B, 386 (1985).

[29] H. Homeyer, M. Burgel, Ch. Egelhaaf, H. Fuchs, and G. Thoma, Z. Phys. A 319, 143 (1984).

[30] G.A. Petitt, A. Gavron, J.R. Beene, B. Cheynis, R.L. Ferguson, F.E. Obenshain, F. Plasil, G.R. Young, M. Jaaskelainen, D.G. Sarantites, and C.F. Maguire, Phys. Rev. C 32, 1572 (1985).

## Table Captions

1) Ratio of alpha particles to protons detected in coincidence with projectile-like fragments of charge Z. The PLF angles at 220 and 341 MeV were $28^{\circ}$ and $16^{\circ}$, respectively.

2) The ratio of M=0 to inclusive yields for projectile-like fragments of charge Z, produced at 220 MeV bombarding energy. The $28^{\circ}$ data are from the present work; the $15^{\circ}$ data are from an earlier $4\pi$ study [9].

## Figure Captions

1) The experimental setup at 220-MeV bombarding energy is illustrated. The phoswich array is centered behind a heavy-ion telescope, with a second telescope positioned symmetrically on the opposite side of the beam. At 341 MeV, the heavy-ion telescopes were positioned at smaller angles ( $\pm$ 16$^{o}$).

2) The multiplicity of light charged particles at 220 MeV is plotted as a function of the charge of the coincident projectile-like fragment. The M=1 yield is decomposed into proton and alpha components, with higher multiplicities also indicated.

3) The distribution of alpha particles observed at 220 MeV in the eight segments of the phoswich array is shown for yields in coincidence with different projectile-like fragments. The asymmetry, A, of the distribution represents the ratio of alpha particles in segments 1-4 to segments 5-8. Also indicated is the position of the heavy-ion telescope. The in-plane angle of the center of each segment may be determined from the top scale.

4) The distribution of alpha particles observed at 341 MeV in the eight segments of the phoswich array is shown for yields in coincidence with different projectile-like fragments. Also shown are the distribution of alpha particles in the "virtual" phoswich array, corresponding to coincidences between phoswich and opposite-side telescope. The position of the same-side heavy-ion telescope is

indicated by the arrow. The in-plane angle of the center of each segment may be determined from the top scale.

5) The differential survival fraction is represented by the M=0/Primary ratios evaluated at the indicated secondary angles. Results are plotted as a function of primary charge, and are derived from the present work ($28^{\circ}$) as well as the earlier $4\pi$ work [9] ($15,20^{\circ}$). The fractions for primary carbon are artificially enhanced because the alpha decay of primary $^{12}C$ leads to three alpha particles in the exit channel.

6) The x-y distribution of alpha particles detected in the phoswich array is shown for the inelastic breakup of $^{20}Ne$ at 220 MeV. The x-coordinate is obtained by randomizing across the width of a phoswich segment. The resulting pattern shows a structure characteristic of sequential decay.

7) The sequential breakup of $^{20}Ne$ at 220 MeV is demonstrated by a plot of energy vs. position for alpha particles detected in each of the eight phoswich segments. This representation is an experimental "slicing" of the breakup sphere.

8) The breakup sphere associated with the sequential decay of $^{20}Ne$ is illustrated. The resulting secondary fragments are detected by the heavy-ion telescope and phoswich array, as shown.

9) The energy spectra of coincident alpha particles and $^{16}O$ fragments are shown at 341 MeV. The heavy ion was detected at 16°, with the coincident alpha particles registered in the phoswich array. The spectra are peaked at energies near beam velocity.

10) The $^{16}O$-$\alpha$ coincidence yield at 341 MeV, represented by the distribution of relative-velocity vectors. Only alpha particles detected in phoswich segment #2 are shown, with the vector decomposed into components parallel and perpendicular to the segment. The shadowing of the phoswich by the heavy-ion telescope is observed at small perpendicular velocities.

11) The energy spectrum of $^{20}Ne$, detected at 28°, is shown for those events in coincidence with a fast proton. The elastic peak corresponds to random coincidences, while the structure at lower energies arises from true coincidences.

12) The spectrum of relative kinetic energy between coincident $^{12}C$ and alpha particles is shown. The energy scale is shifted by the separation energy, to correspond to excitation in primary $^{16}O$. The shaded region extending up to the alpha-decay threshold represents the yield of primary $^{16}O$ produced in particle-bound states. Arrows indicate the positions of the proton and neutron thresholds. Also displayed are results from a Monte Carlo calculation of the detection efficiency for alpha particles emitted in coincidence with a detected $^{12}C$ ejectile, as a function of the relative kinetic energy between the secondary fragments.

13) The spectrum of relative kinetic energy between coincident $^{13}C$ and alpha particles is shown. The energy scale is shifted by the separation energy, to correspond to excitation in primary $^{17}O$. The shaded region extending up to the neutron-decay threshold represents the yield of primary $^{17}O$ produced in particle-bound states. Arrows also indicate the positions of the proton and alpha thresholds, as well as the threshold for sequential $\alpha n$ emission.

14) The reconstructed primary excitation distributions are plotted for eight different channels, ranging from two-neutron pickup to alpha stripping. Reconstructions were made from the relative-energy spectra derived from alpha emission. The shaded regions represent the particle-bound yields.

15) The branching ratios for neutron and alpha decay of $^{22}Ne$ are plotted as a function of excitation energy. Calculations were performed with the statistical-model code STATIS [15], and employed transmission coefficients derived from optical-model calculations.

16) The three-body Q-value spectra derived from kinematic reconstructions of coincidence data are shown for eight different primary binary channels, ranging from two-neutron pickup to alpha stripping. The energy scale is shifted by the ground-state Q-value, to correspond to excitations in the primary target-like fragments.

17) Contour plots of reconstructed projectile-like vs. target-like excitation energies are shown for two specific primary channels, corresponding to pn stripping and 2n pickup. Reconstructions were performed from the coincident alpha events. The position of the alpha-decay threshold in the projectile-like fragment is indicated by the thin solid line.

18) The excitation-energy distribution in primary $^{16}O^*$ is compared at bombarding energies of 220 and 341 MeV. The relative-energy spectra deduced from $^{12}C$-$\alpha$ coincidences are shifted by the separation energy (dashed line), and the position of the lowest alpha-decaying state is indicated by the arrow.

19) The TLF excitation-energy distributions for the primary $^{16}O^*$ channel are compared for bombarding energies of 220 and 341 MeV. The Q-value spectra deduced from $^{12}C$-$\alpha$ coincidences are shifted by the ground-state Q-value.

20) Most-probable TLF excitations, as deduced from three-body kinematic reconstructions, are shown at both bombarding energies. The primary channels are specified by the associated PF.

21) Reconstructed PF excitations at 220 MeV deduced from $\alpha$-PLF coincidences via the relation $E_x(PF) = E_{rel} + S_\alpha$ . The channels shown are (a) $\alpha$ stripping, (b) pn stripping, (c) inelastic scattering, and (d) 2n pickup. Particle-bound yields below threshold (dashed line) are represented as fractions of the reconstructed

primary yields. Arrows indicate the positions of the first state (or cluster of states) above threshold.

22) Reconstructed TLF excitations at 220 MeV deduced from $\alpha$-PLF coincidences. Calculations employ three-body kinematics to evaluate $Q_3$ in the relation $E_x(TLF) = Q_{ggg} - Q_3$ . The primary channels are as in Fig. 21. Arrows indicate the total excitations predicted by the model of Siemens et al. [17].

23) Comparison of experimental TLF excitation energies (most-probable values) obtained at 220 MeV with calculations based on optimum Q-values. The open circles and squares represent calculations assuming uni-directional and bi-directional mass transfer, respectively.

24) Comparison of experimental TLF excitation energies (most-probable values) obtained at 341 MeV with calculations based on optimum Q-values. The open circles and squares represent calculations assuming uni-directional and bi-directional mass transfer, respectively.

α/p ratios

| $Z_{PLF}$ | 220 MeV | 341 MeV |
|---|---|---|
| 3 | 13.0 ± 3.1 | 3.41 ± 0.19 |
| 4 | 10.4 ± 2.1 | 2.37 ± 0.20 |
| 5 | 11.2 ± 1.5 | 2.82 ± 0.18 |
| 6 | 8.1 ± 0.4 | 2.14 ± 0.07 |
| 7 | 24.1 ± 1.5 | 3.96 ± 0.16 |
| 8 | 13.1 ± 0.4 | 3.63 ± 0.09 |
| 9 | 0.21 ± 0.04 | 0.36 ± 0.02 |

Table 1

$$R(Z_{PLF}, \theta_{PLF}) = \sigma_{M=0}/\sigma_{inclusive}$$

| $Z_{PLF}$ | $R\ (\theta_{PLF}=28^{o})$ | $R\ (\theta_{PLF}=15^{o})$ |
|---|---|---|
| 3 | 0.86 | -- |
| 4 | 0.83 | 0.59 |
| 5 | 0.80 | 0.57 |
| 6 | 0.73 | 0.54 |
| 7 | 0.63 | 0.65 |
| 8 | 0.77 | 0.81 |
| 9 | 0.99 | 0.95 |

Table 2

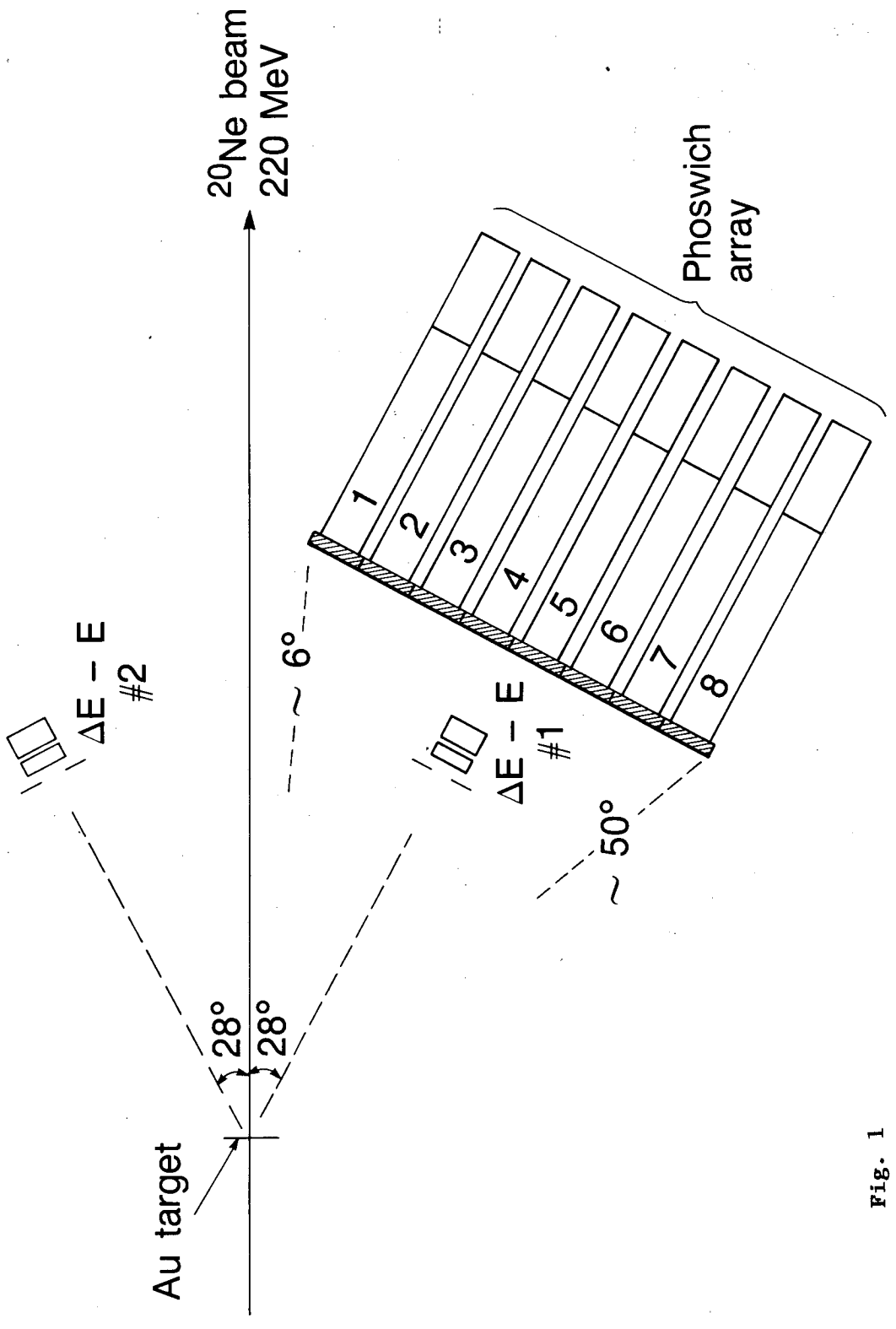


XBL 867-9853

Fig. 1

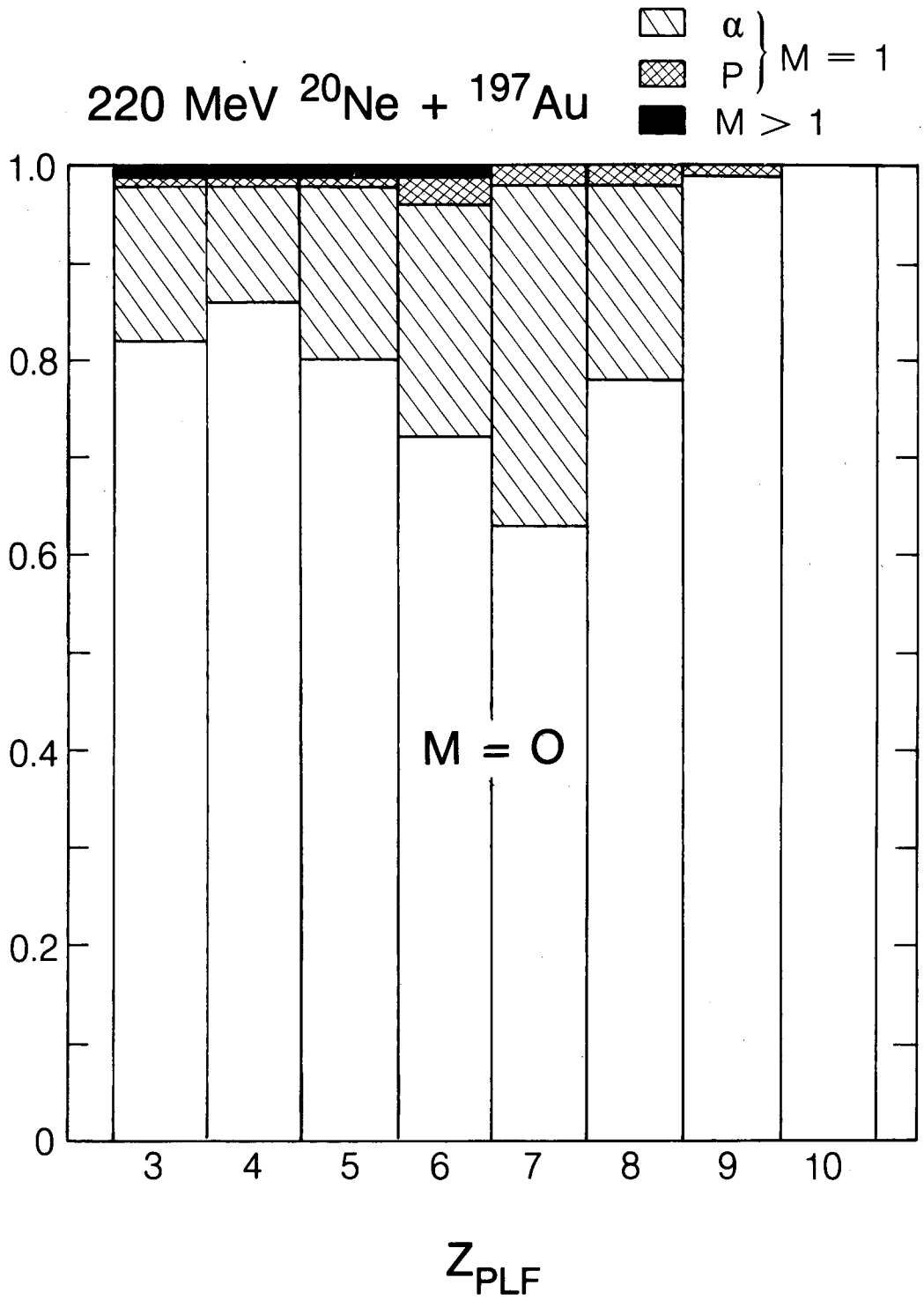


Fig. 2

XBL 786-11641

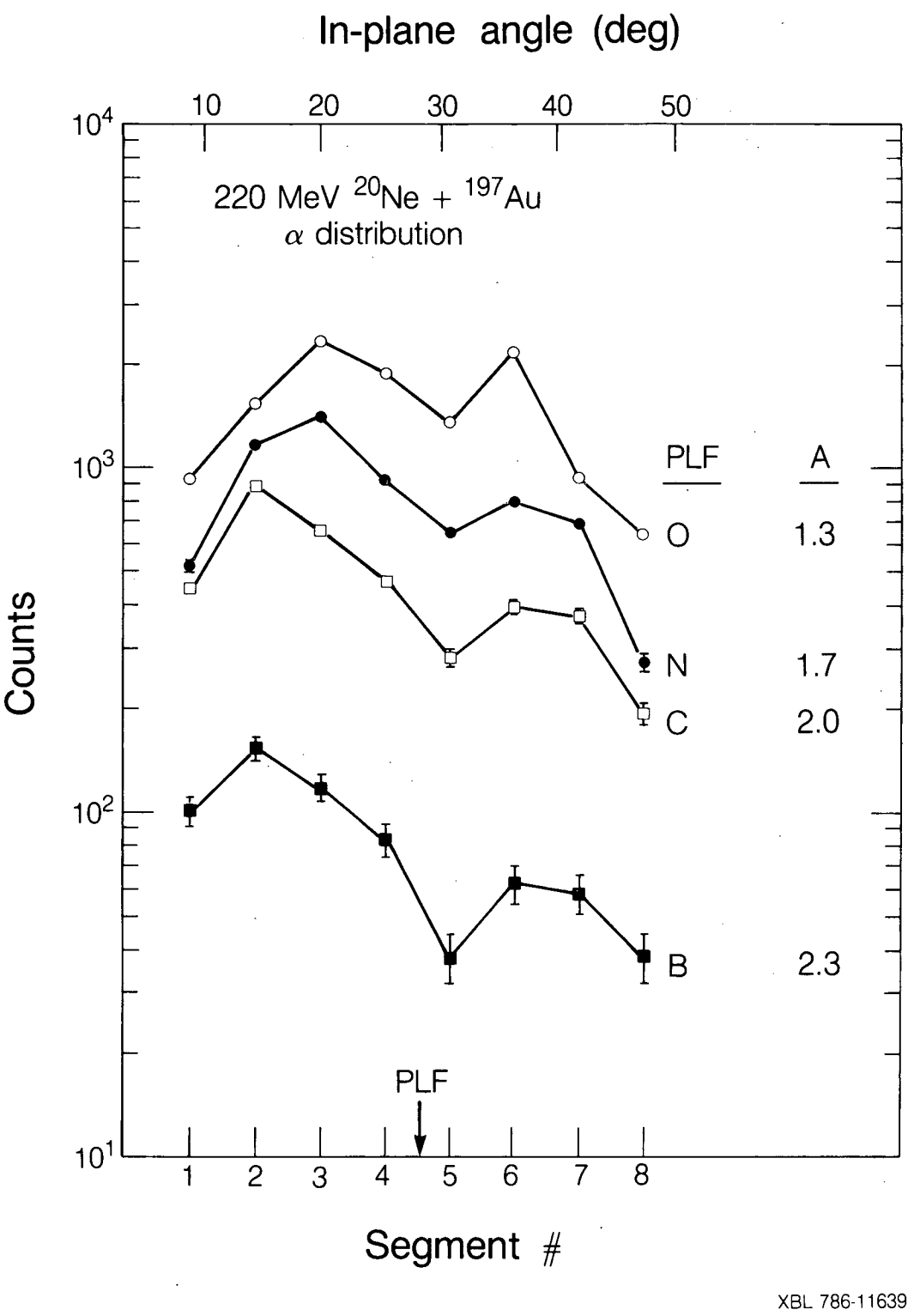
In-plane angle (deg)
10
20
30
40
50
$10^4$
$10^3$
$10^2$
$10^1$
220 MeV $^{20}$Ne + $^{197}$Au
$\alpha$ distribution
PLF
A
O
1.3
N
1.7
C
2.0
B
2.3
Counts
PLF
1
2
3
4
5
6
7
8
Segment #
XBL 786-11639

**Fig. 3.**

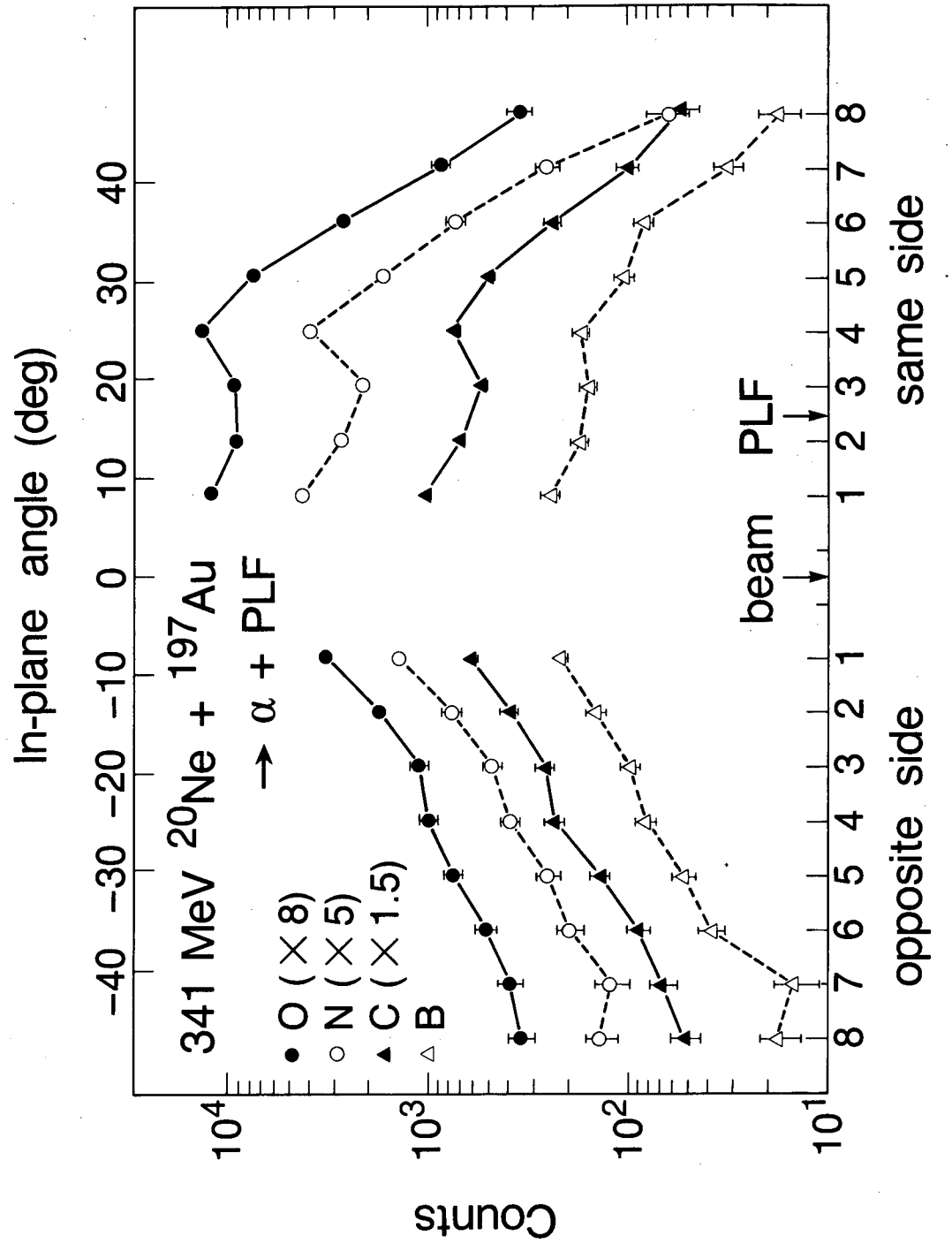


XBL 867-11202

Fig. 4

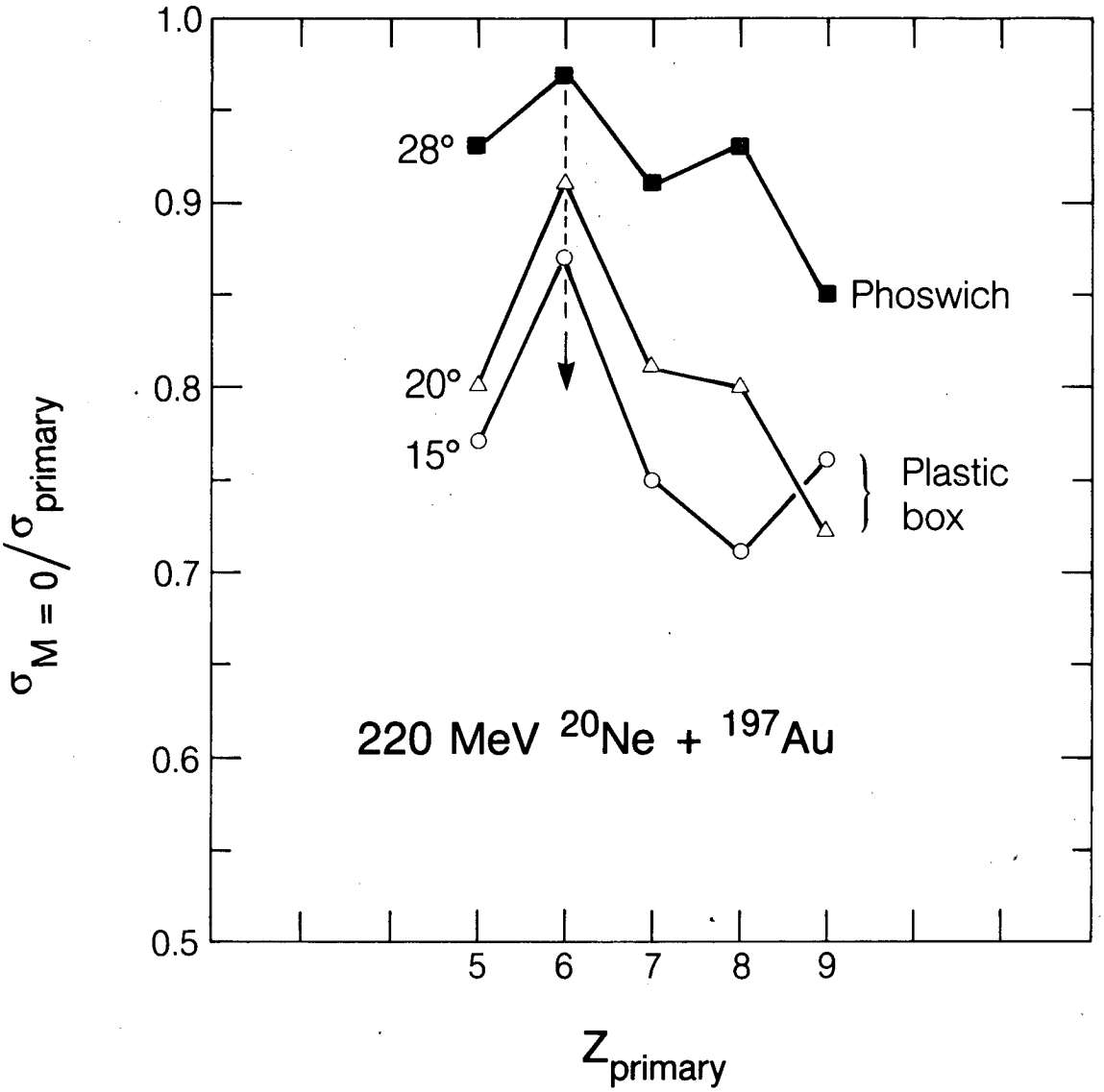


XBL 786-11642

Fig.5

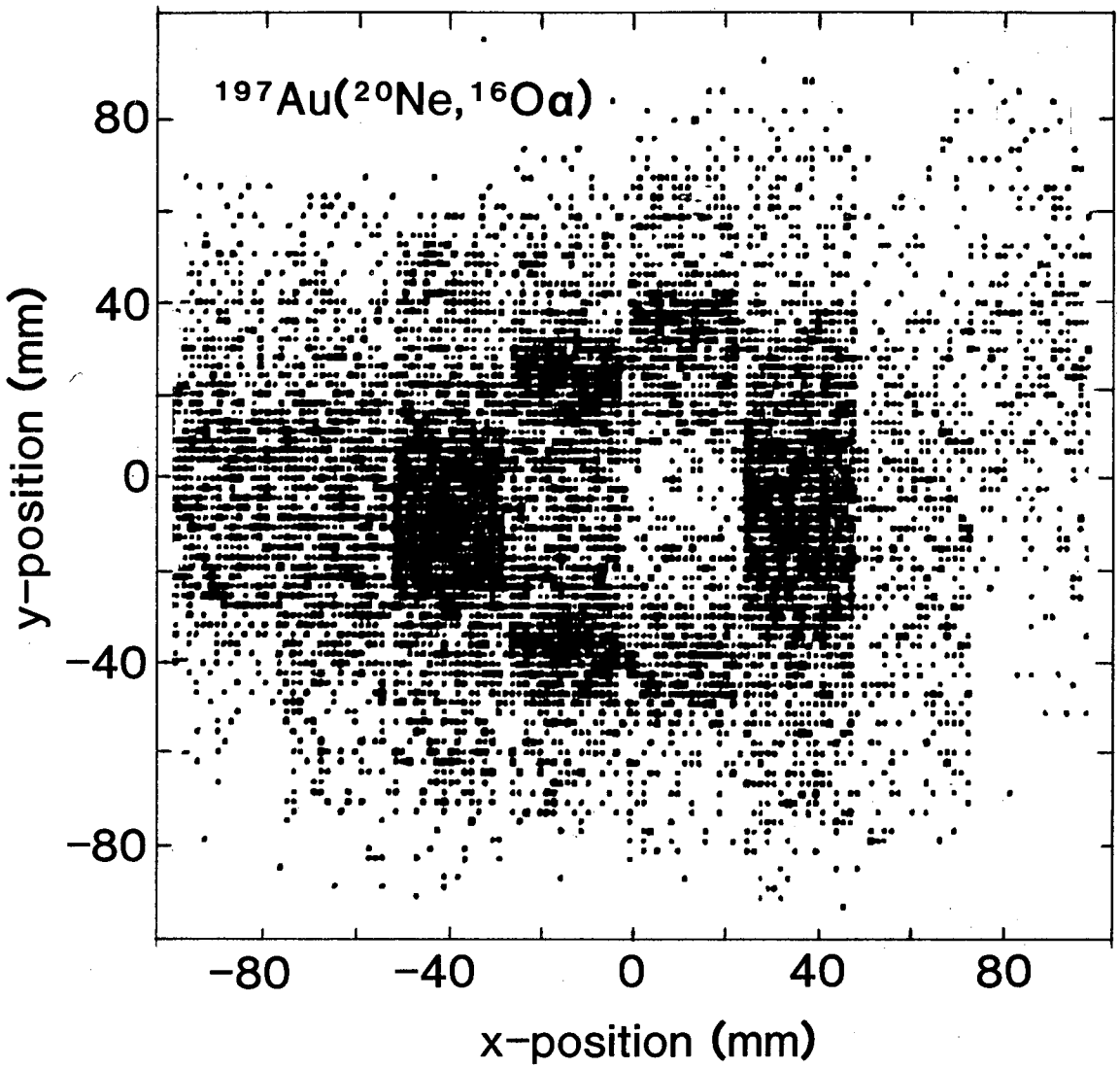


XBL 855-2329

Fig. 6

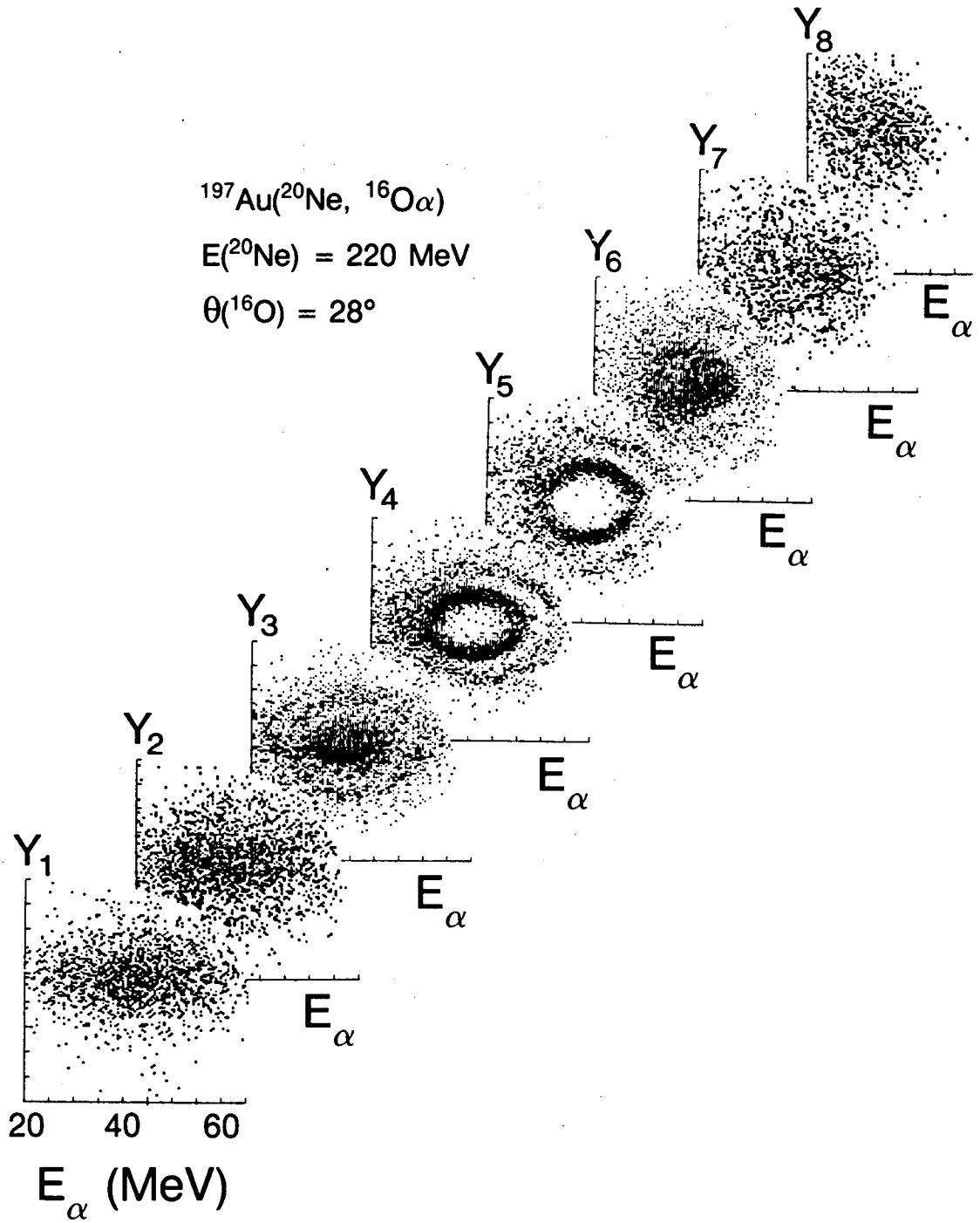


XBL 855-2482

Fig. 7

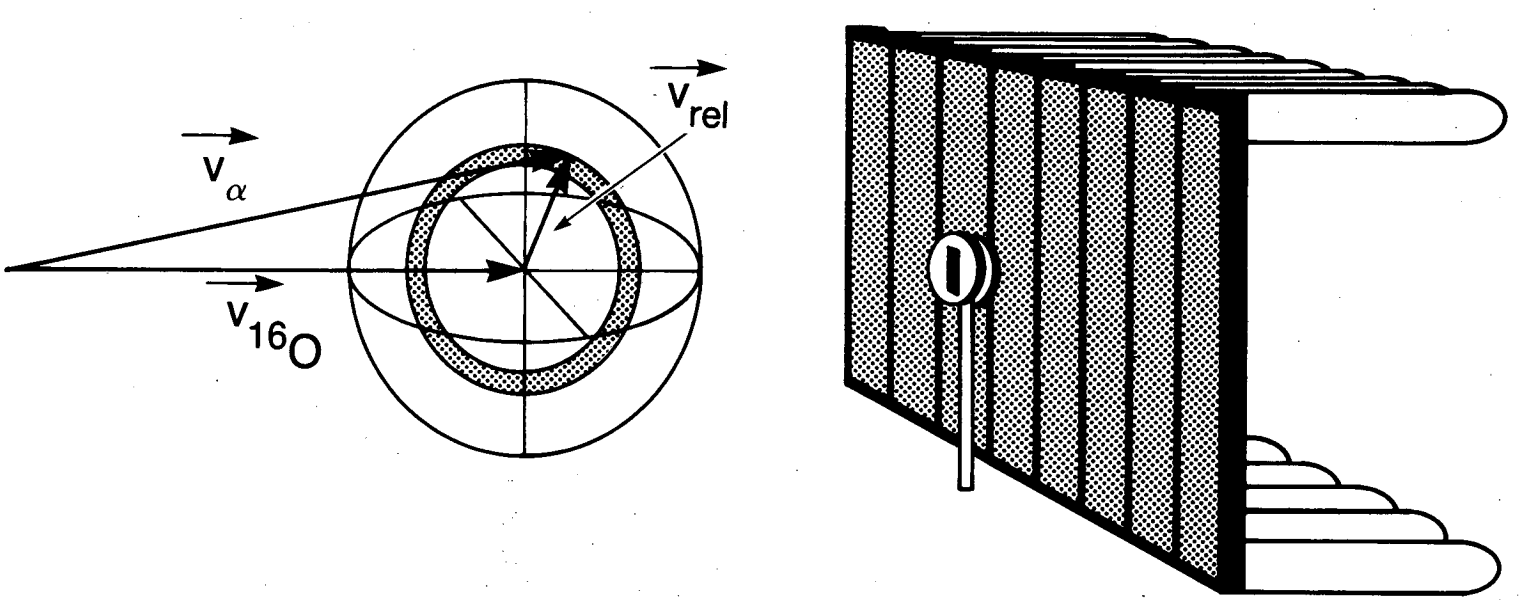


XBL 786-11645

**Fig. 8**

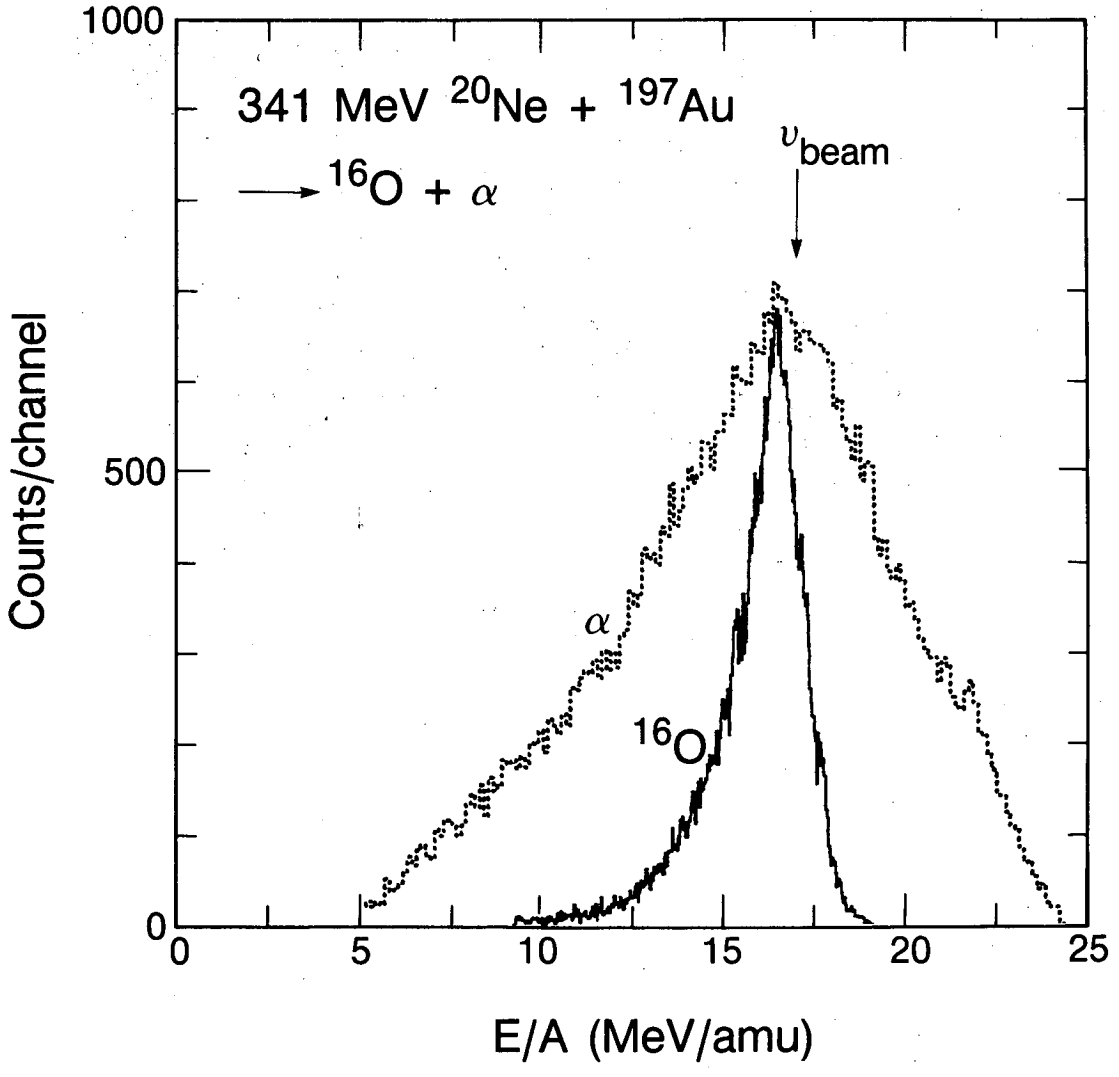


XBL 867-11193

Fig. 9

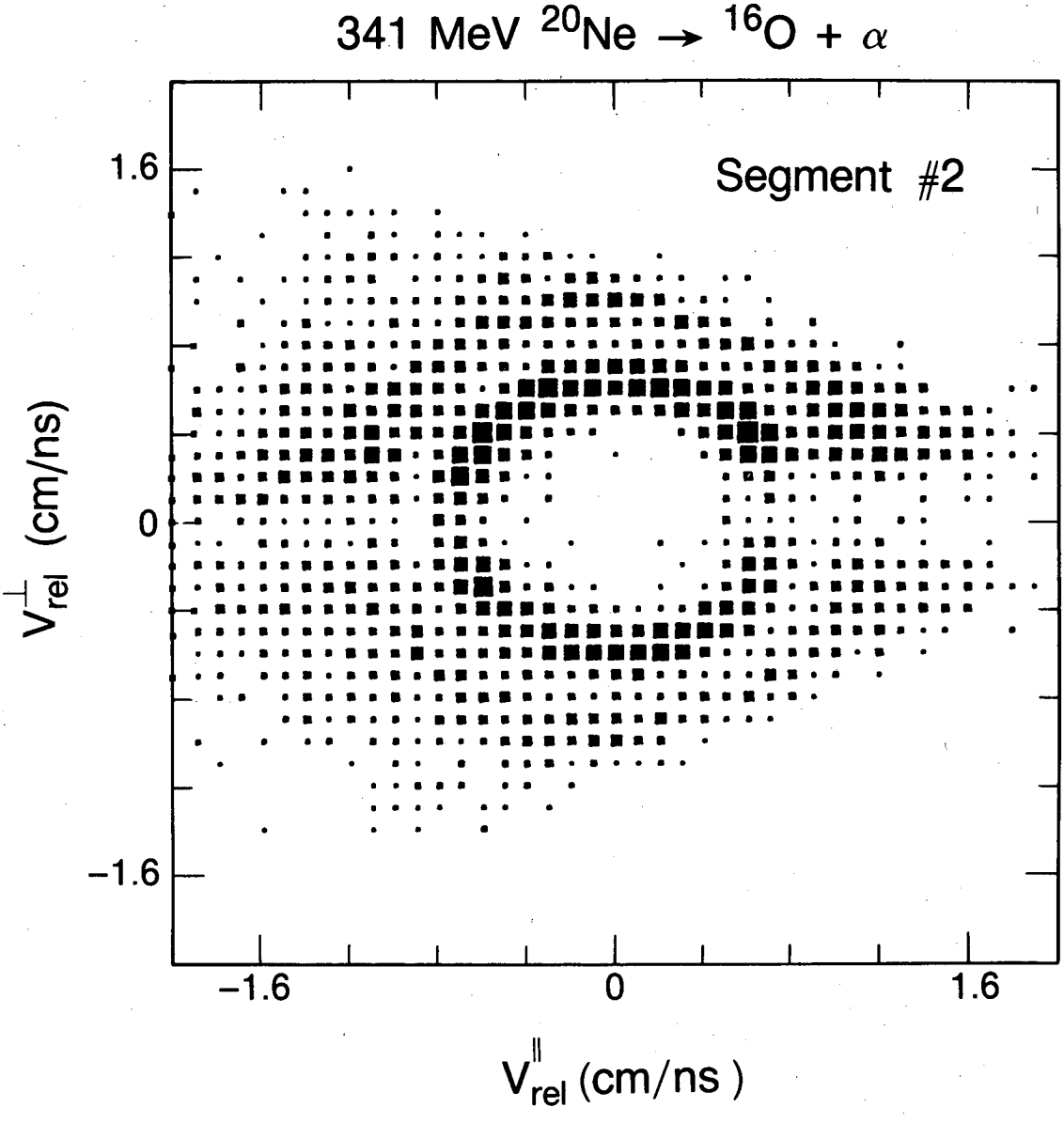


XBL 867-11195

Fig. 10

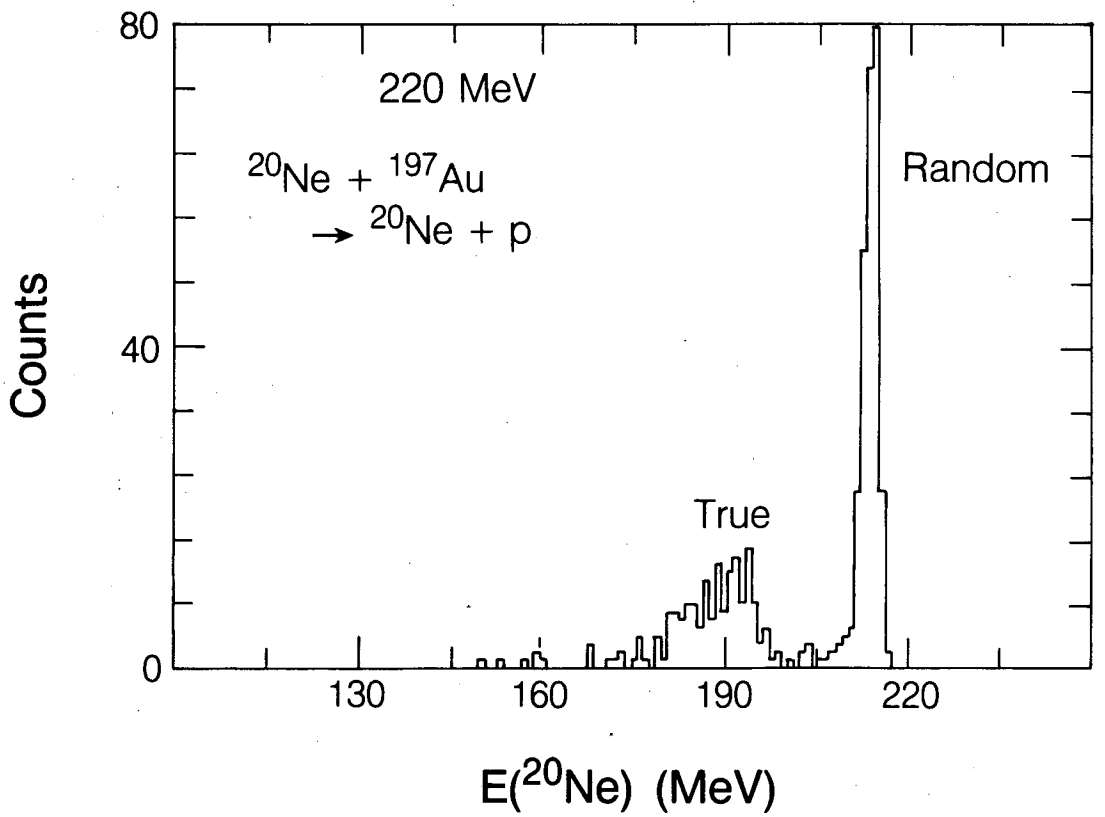


XBL 786-11640

**Fig. 11**

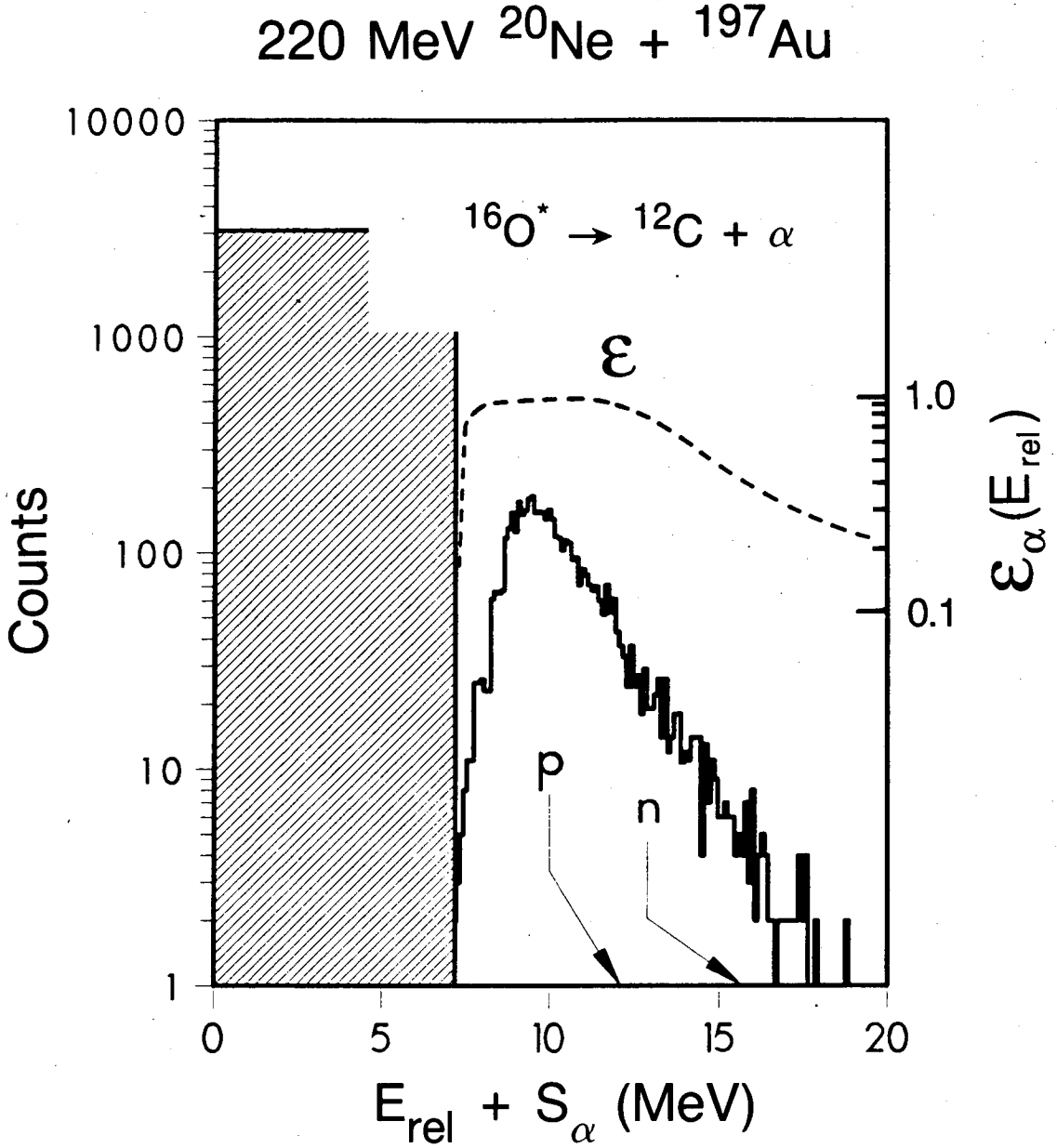


XBL 862-469A

**Fig. 12**

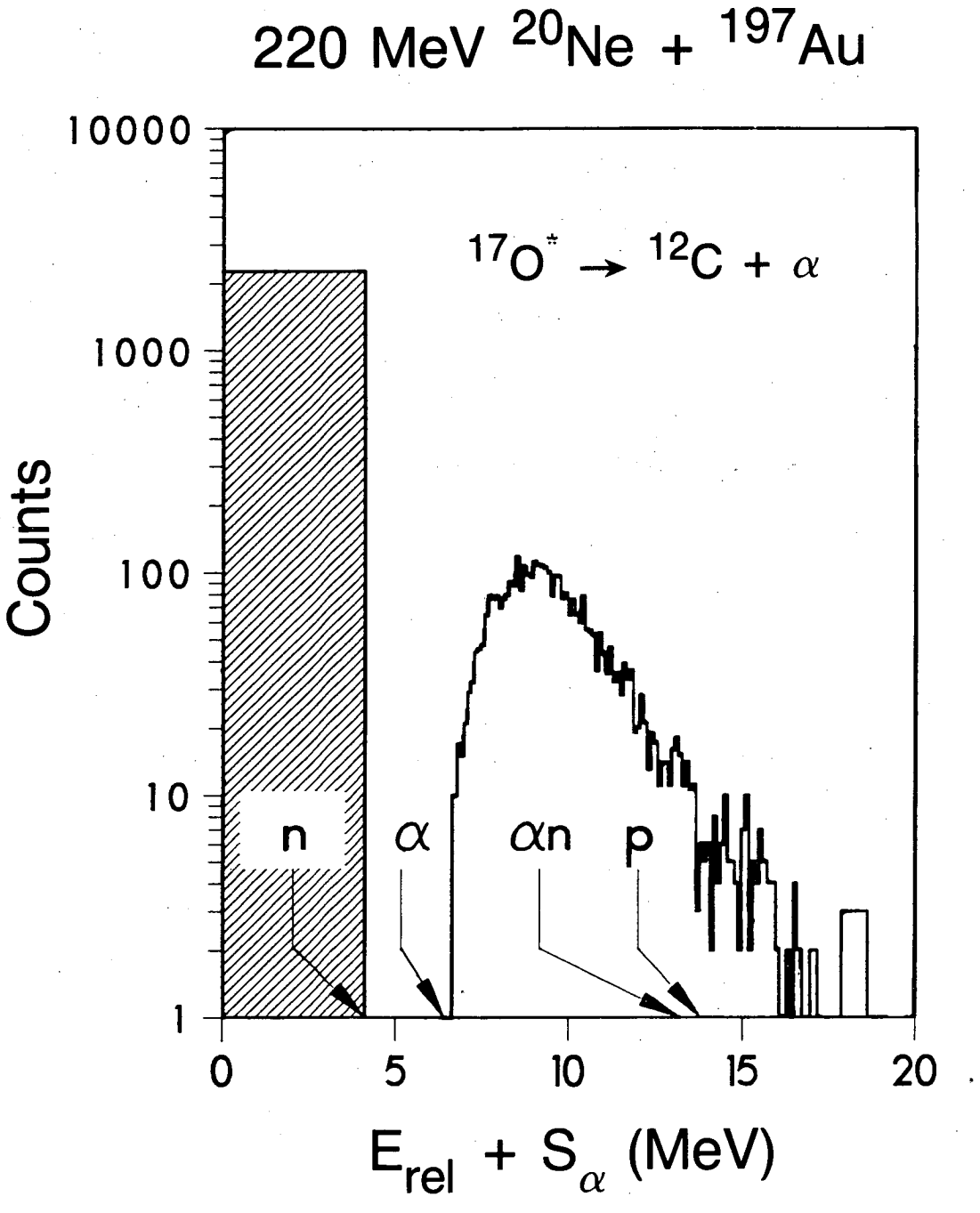
220 MeV $^{20}$Ne + $^{197}$Au
$^{17}O^{*} \rightarrow {}^{12}C + \alpha$
Counts
10000
1000
100
10
1
n
α
αn
p
0
5
10
15
20
$E_{rel} + S_{\alpha}$ (MeV)
XBL 862-449

Fig. 13

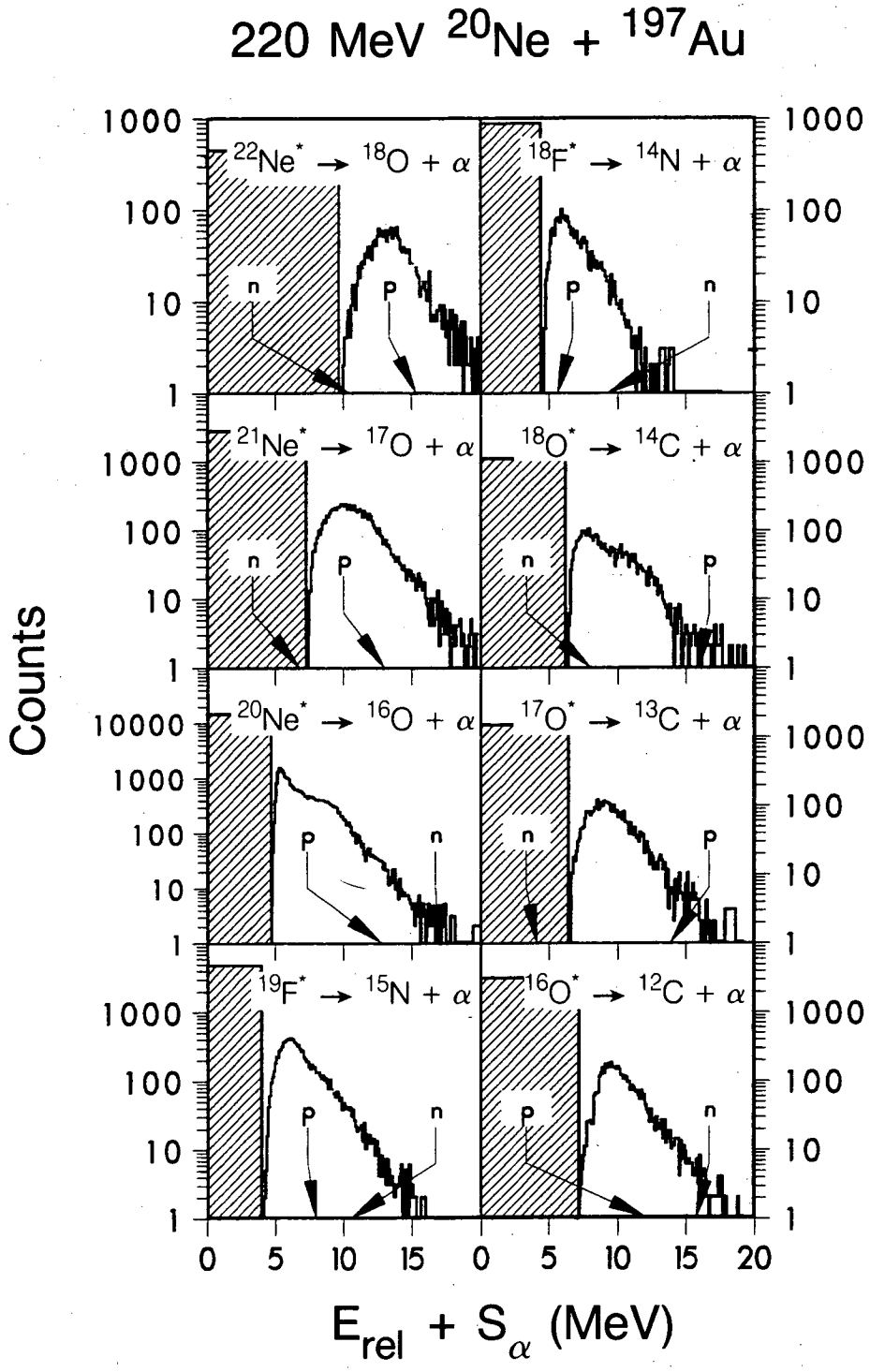
220 MeV $^{20}$Ne + $^{197}$Au
$^{22}$Ne* → $^{18}$O + α
$^{18}$F* → $^{14}$N + α
$^{21}$Ne* → $^{17}$O + α
$^{18}$O* → $^{14}$C + α
$^{20}$Ne* → $^{16}$O + α
$^{17}$O* → $^{13}$C + α
$^{19}$F* → $^{15}$N + α
$^{16}$O* → $^{12}$C + α
n
p
Counts
$E_{rel}$ + $S_\alpha$ (MeV)
XBL 8510-4346

**Fig. 14**

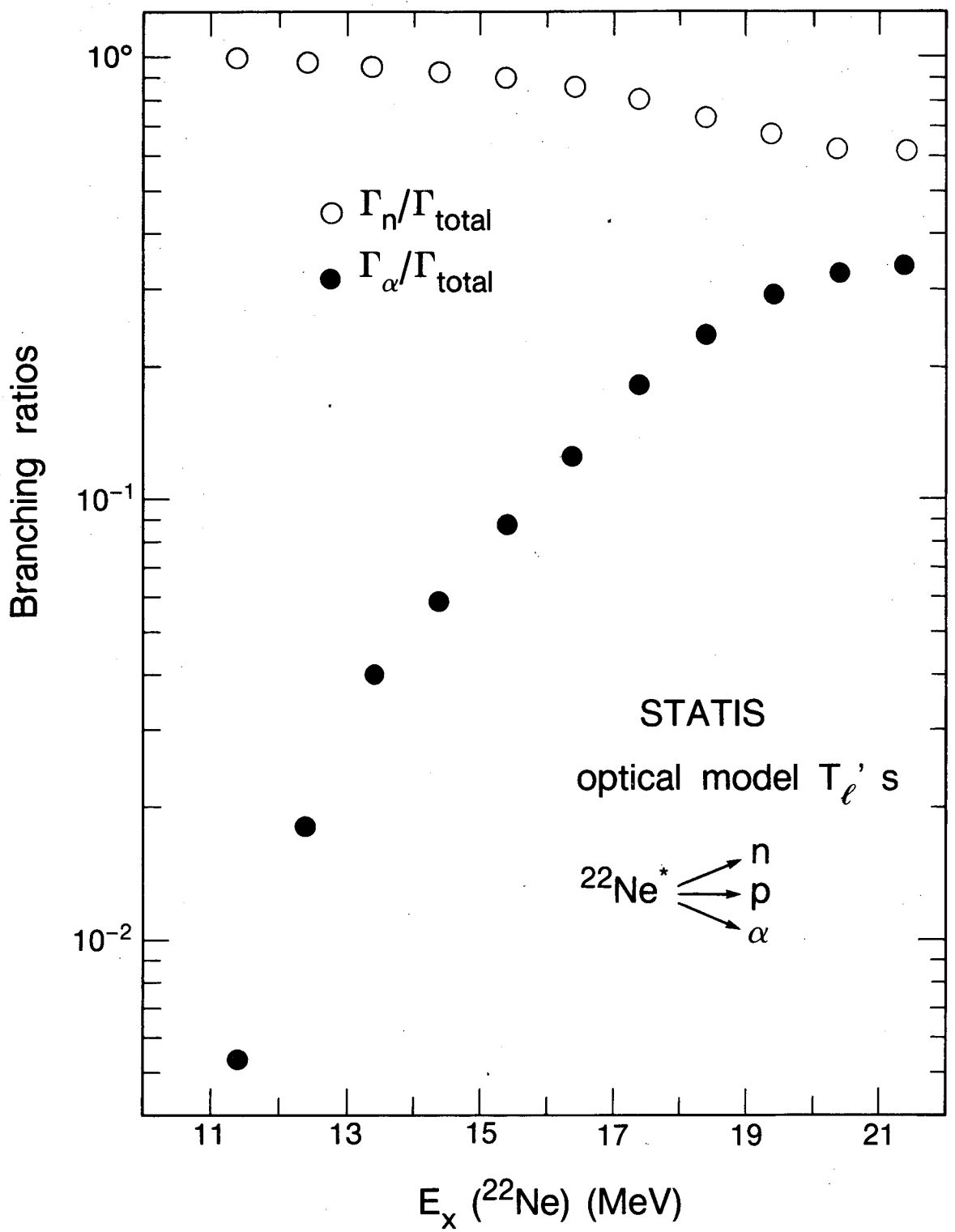


XBL 867-11196

Fig. 15

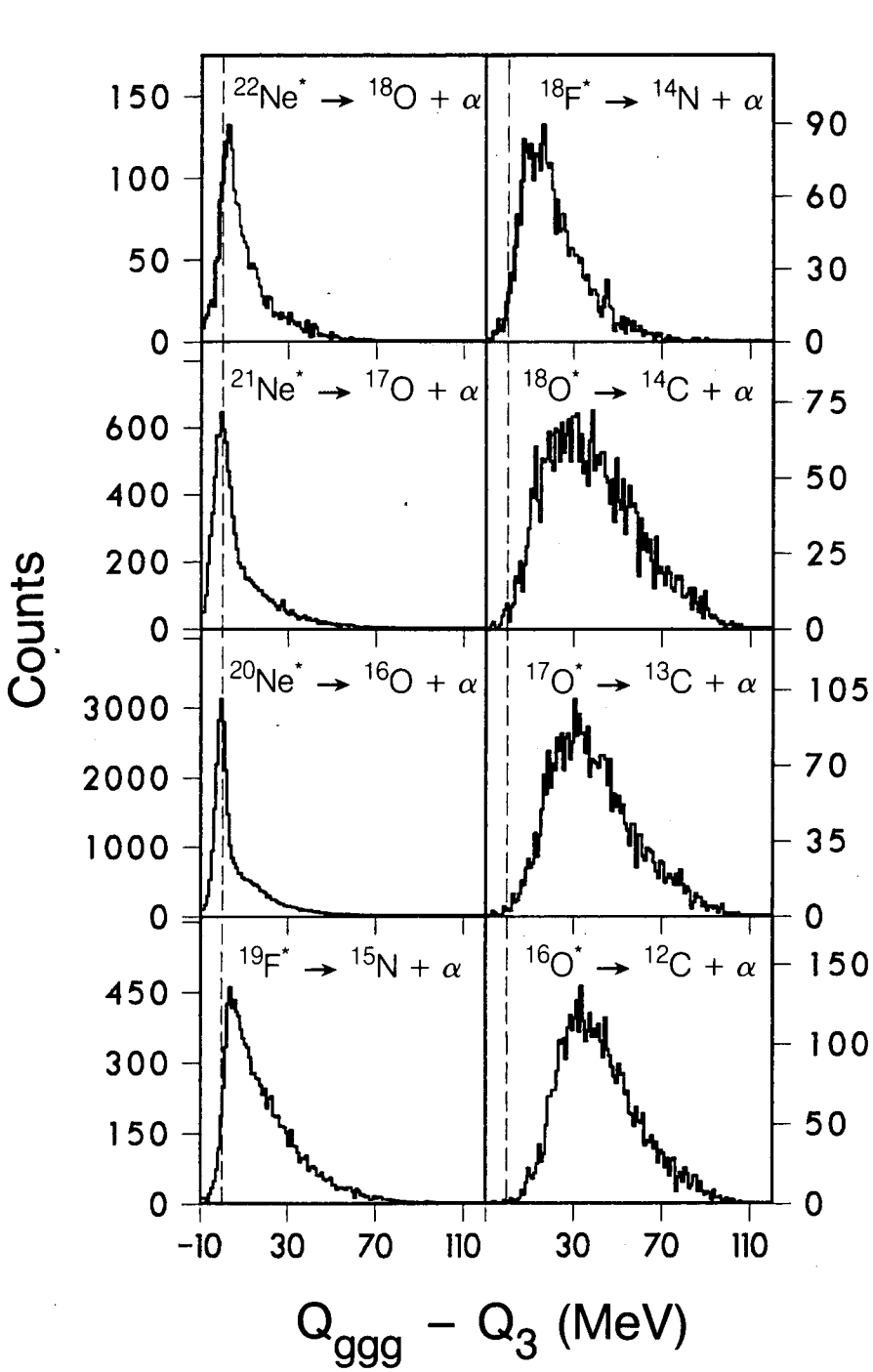


XBL 8510-4344

**Fig. 16**

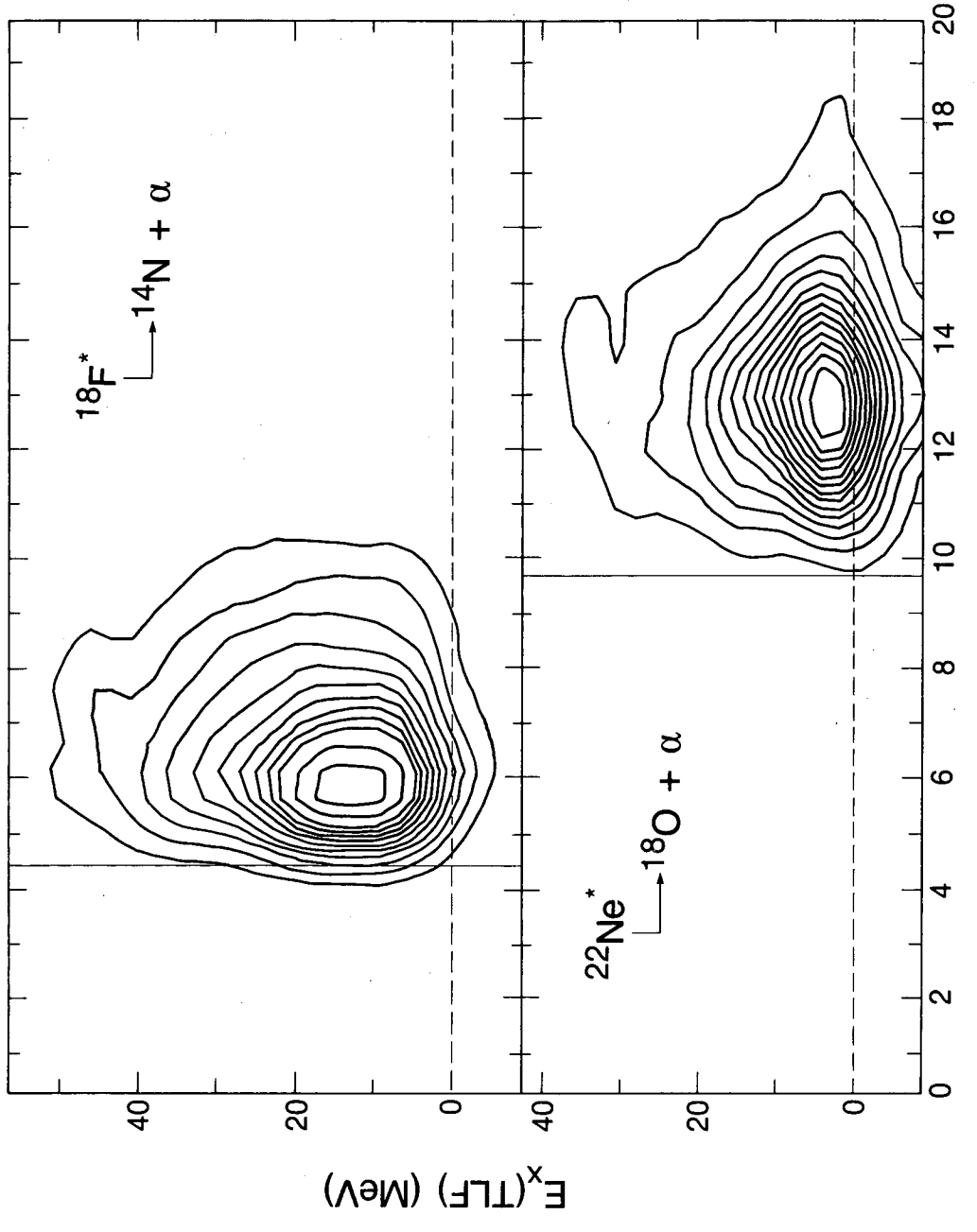


XBL 867-11197

**Fig. 17**

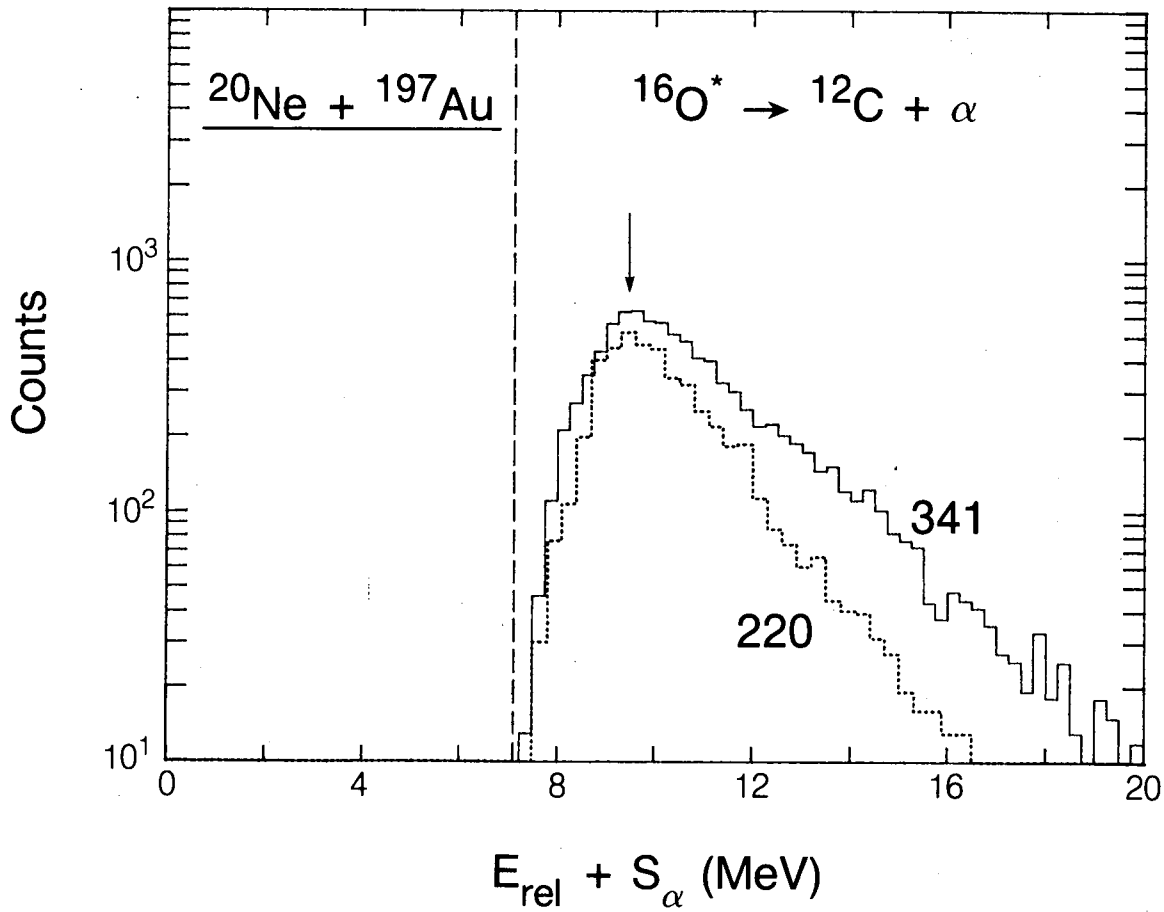


XBL 868-11222

**Fig. 18**

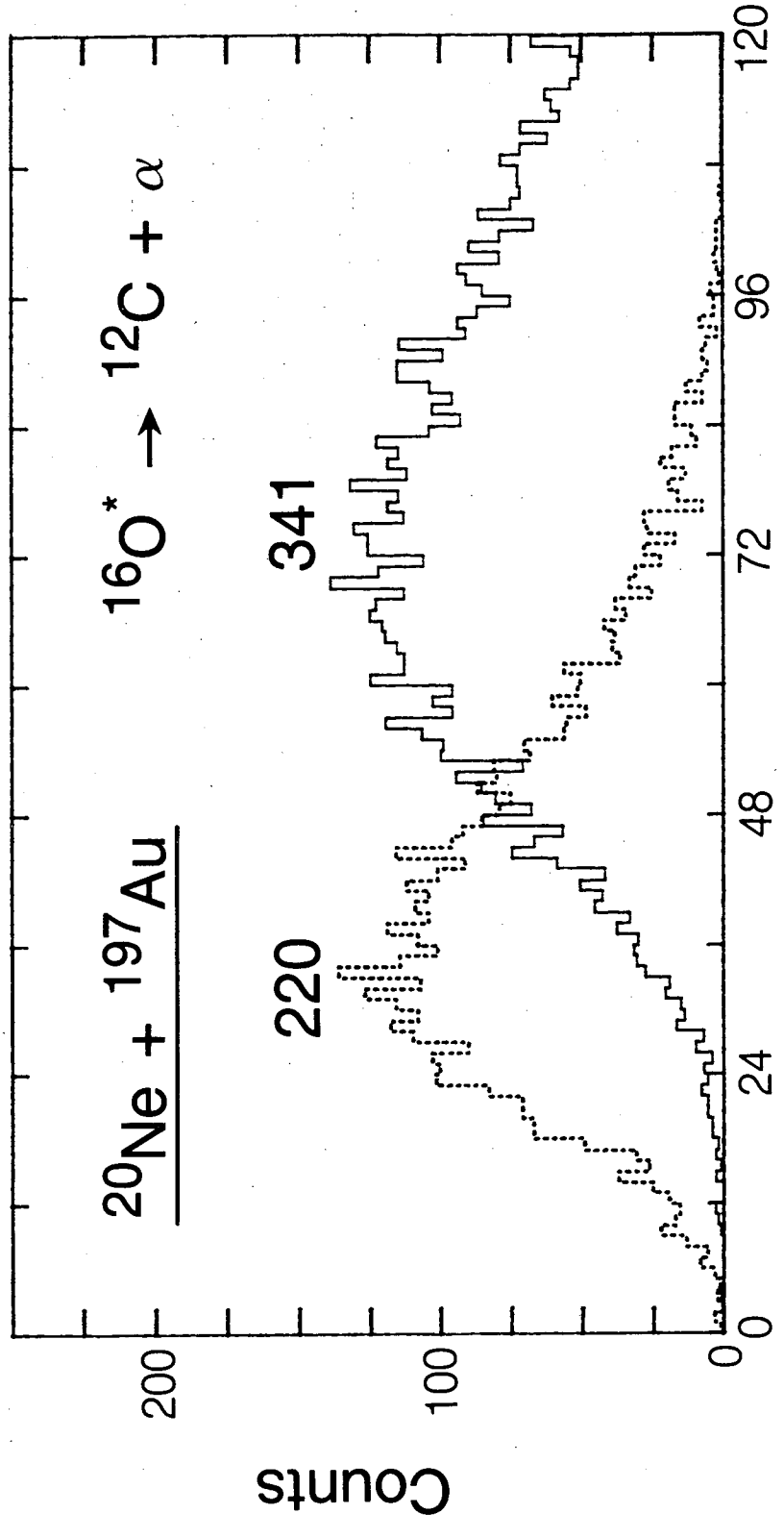


XBL 868-11223

Fig. 19

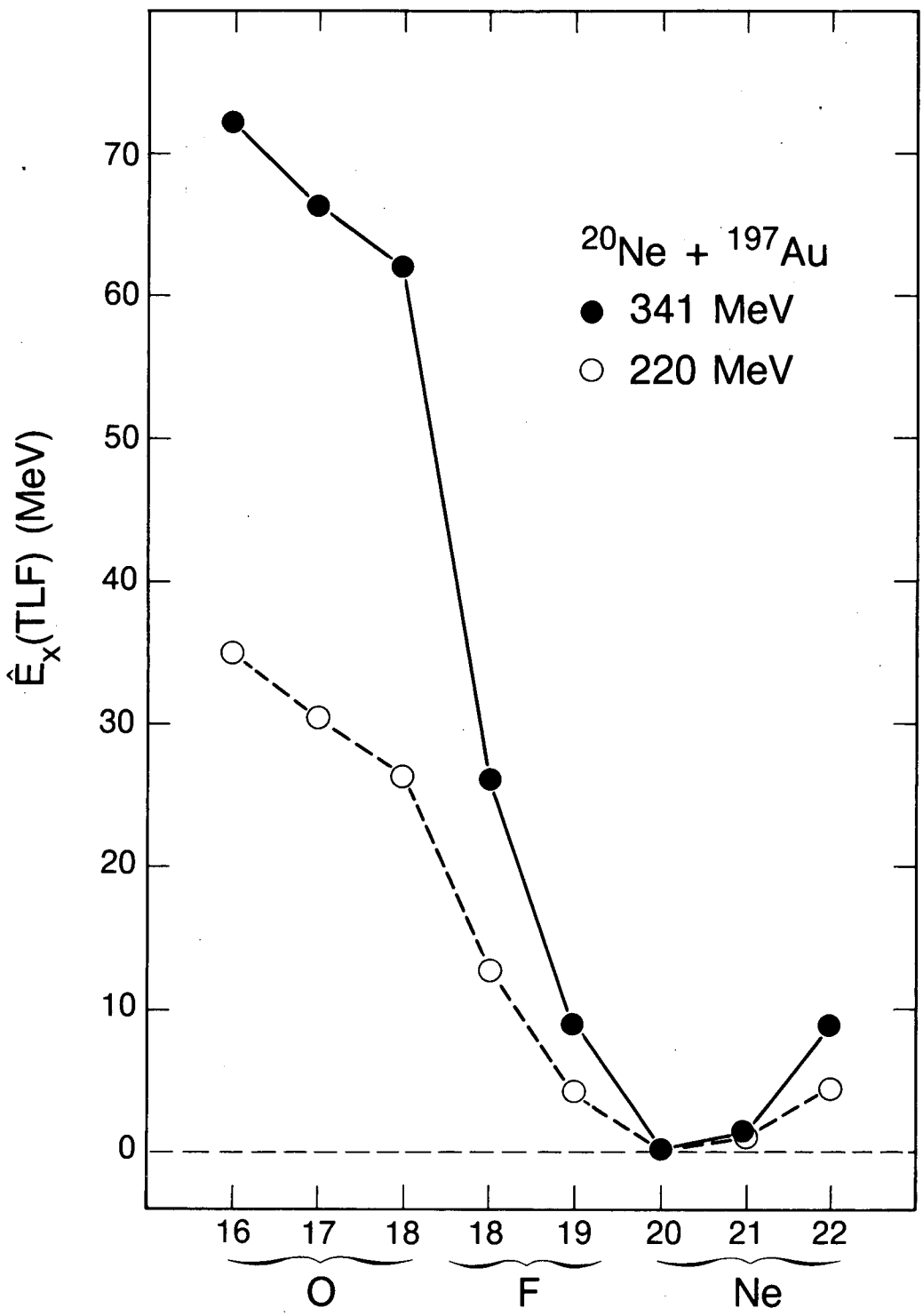


Fig. 20

XBL 867-11192

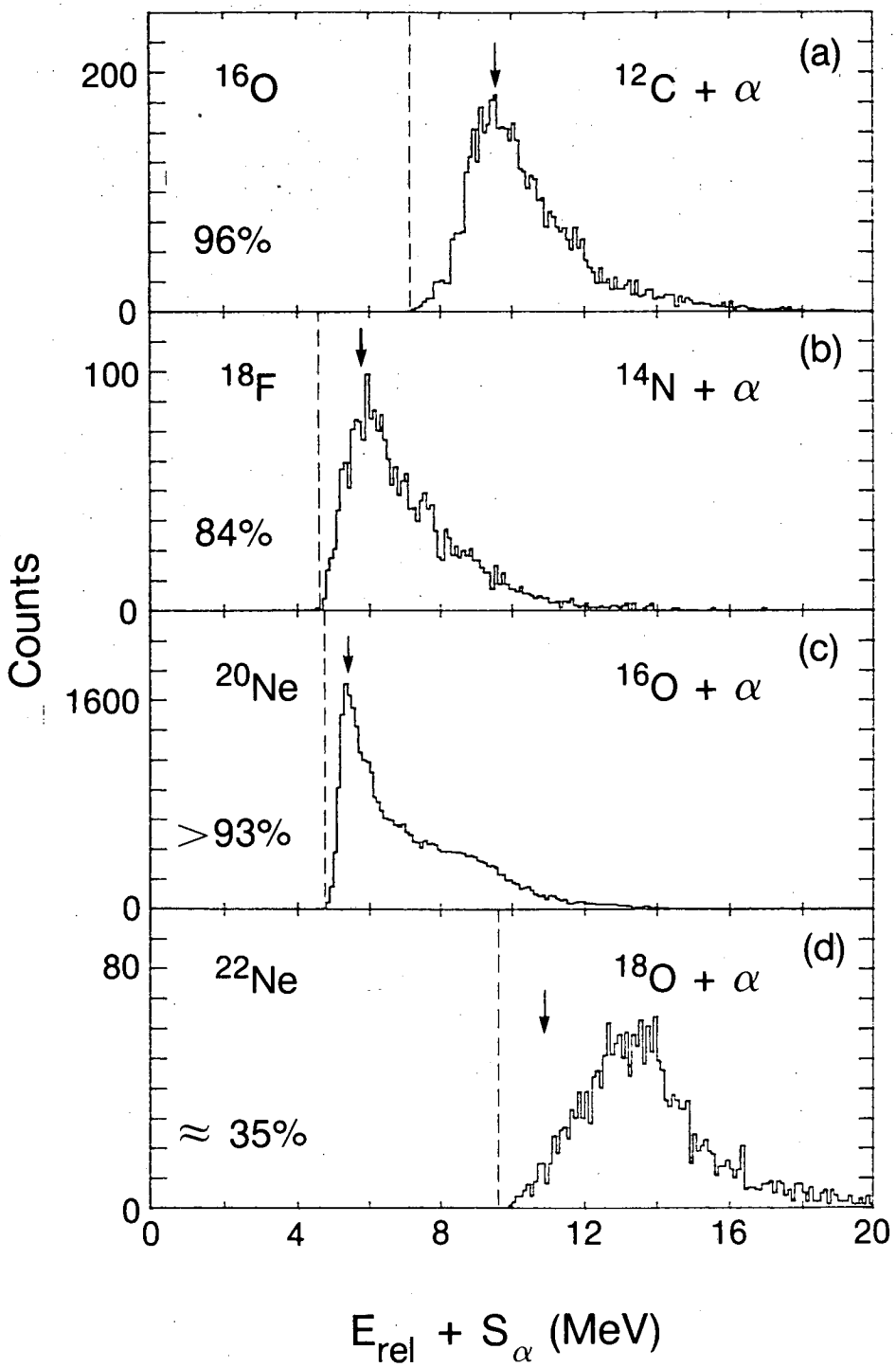


**Fig. 21**

XBL 866-10447

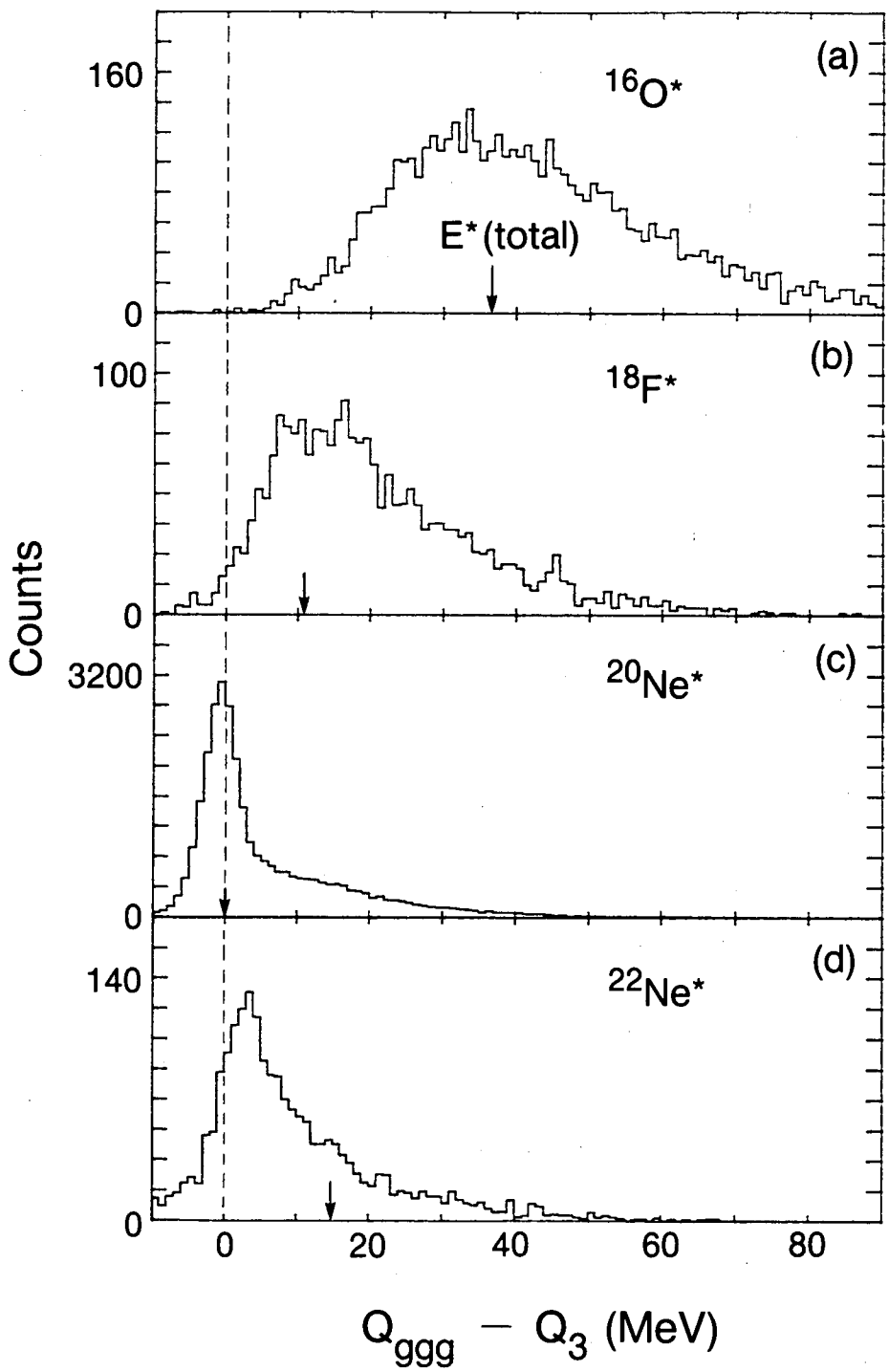


XBL 866-10446

Fig. 22

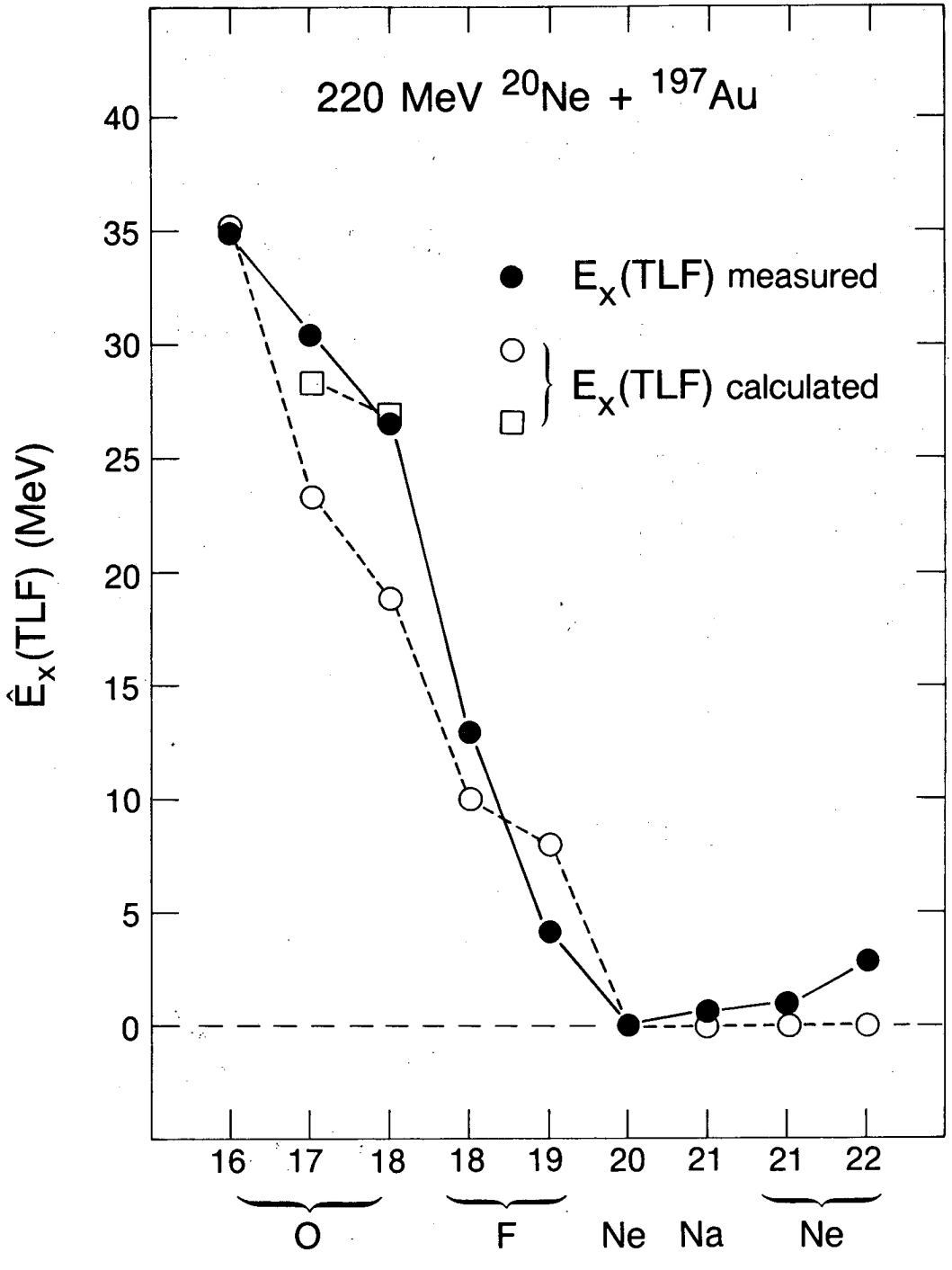


XBL 866-10445

Fig. 23

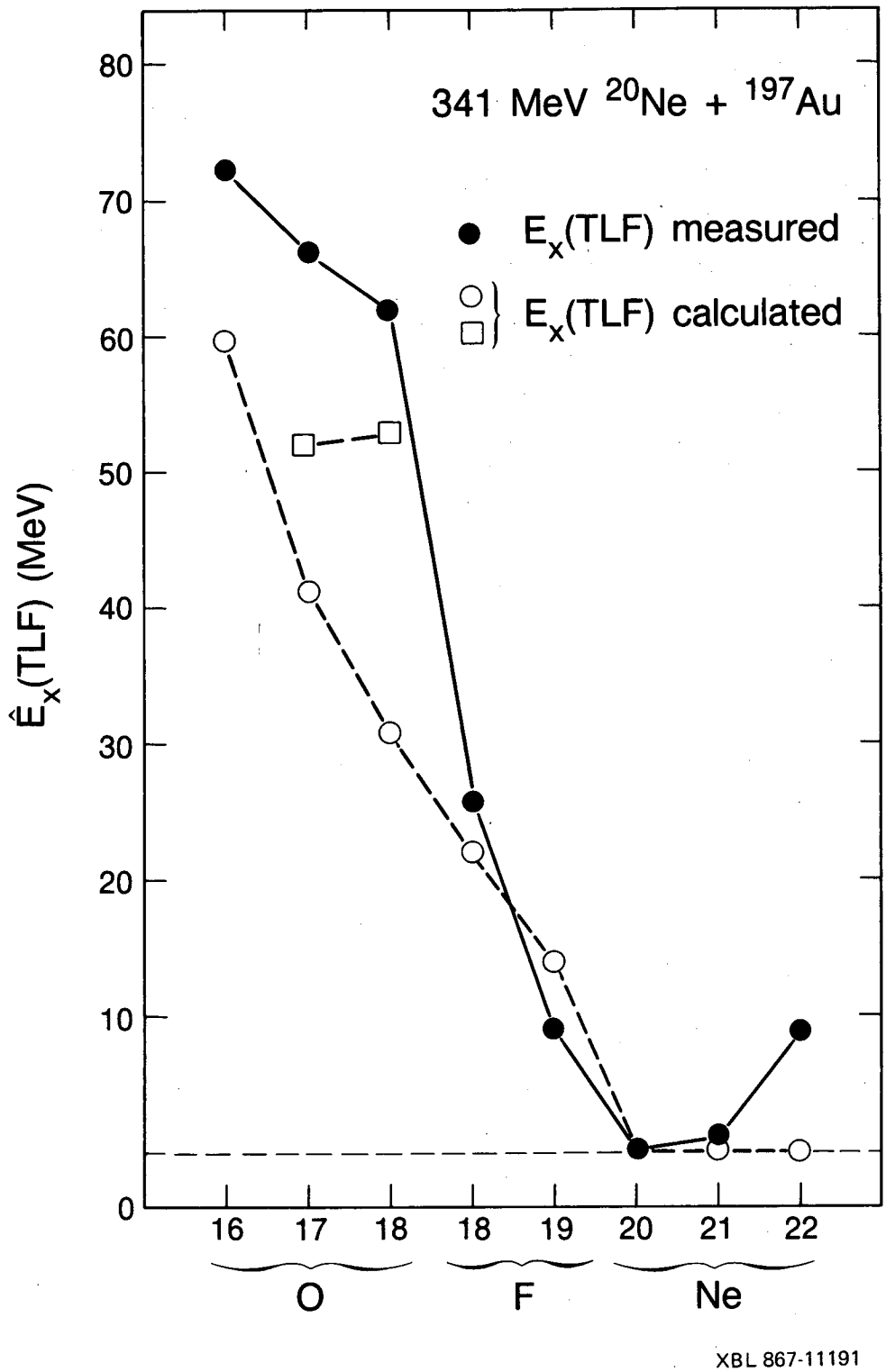
341 MeV $^{20}$Ne + $^{197}$Au
$E_x$(TLF) measured
$E_x$(TLF) calculated
$\hat{E}_x$(TLF) (MeV)
0
10
20
30
40
50
60
70
80
16
17
18
18
19
20
21
22
O
F
Ne
XBL 867-11191

Fig. 24

*LAWRENCE BERKELEY LABORATORY*
*TECHNICAL INFORMATION DEPARTMENT*
*UNIVERSITY OF CALIFORNIA*
*BERKELEY, CALIFORNIA 94720*